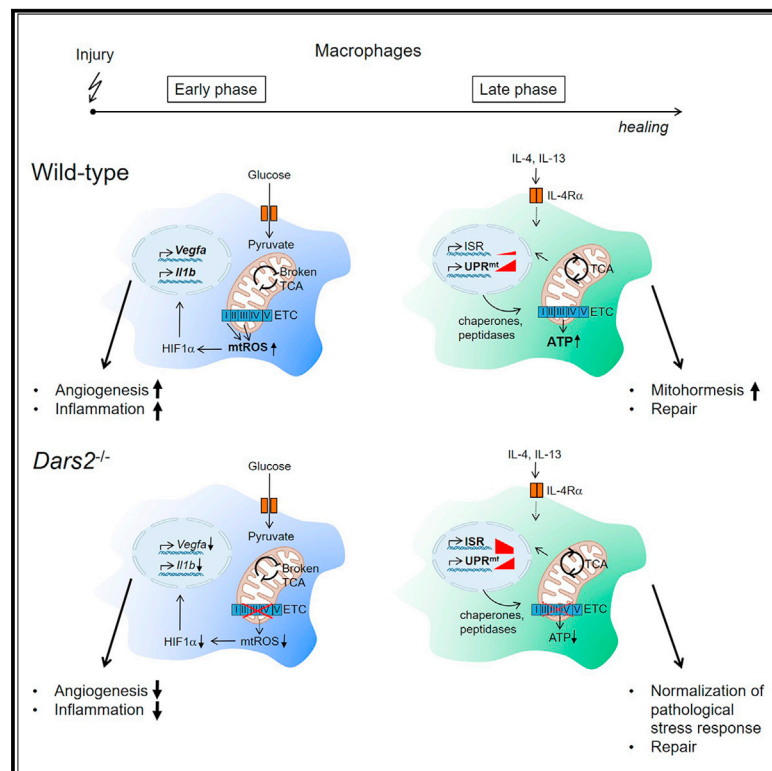


# Cell Metabolism

## Mitochondrial metabolism coordinates stage-specific repair processes in macrophages during wound healing

### Graphical abstract



### Authors

Sebastian Willenborg, David E. Sanin, Alexander Jais, ..., Jens C. Brünig, Aleksandra Trifunovic, Sabine A. Eming

### Correspondence

sabine.eming@uni-koeln.de

### In brief

How mitochondrial metabolism contributes to the early-stage, pro-inflammatory versus late-stage, pro-resolution functions of macrophages during wound healing requires further investigation. Here, Willenborg et al. show that effective wound healing requires the production of mtROS in early-stage wound macrophages to promote proper vascularization, while late-stage wound macrophages are dependent on OXPHOS and mitohormesis.

### Highlights

- Early-stage, inflammatory versus late-stage, pro-resolving wound macrophages are profiled
- Pro-inflammatory wound macrophages are marked by mtROS production and HIF1 $\alpha$  stabilization
- This molecular process is required for proper vascularization during wound repair
- Pro-resolving macrophages are marked by mitochondrial respiration and mitohormesis



Article

# Mitochondrial metabolism coordinates stage-specific repair processes in macrophages during wound healing

Sebastian Willenborg,<sup>1</sup> David E. Sanin,<sup>2</sup> Alexander Jais,<sup>3,4</sup> Xiaolei Ding,<sup>1</sup> Thomas Ulas,<sup>5,6</sup> Julian Nüchel,<sup>7</sup> Milica Popović,<sup>8</sup> Thomas MacVicar,<sup>9</sup> Thomas Langer,<sup>9,10,11</sup> Joachim L. Schultze,<sup>5,6</sup> Alexander Gerbaulet,<sup>12</sup> Axel Roers,<sup>12</sup> Edward J. Pearce,<sup>2,13</sup> Jens C. Brüning,<sup>3,10,11</sup> Aleksandra Trifunovic,<sup>8,10,11</sup> and Sabine A. Eming<sup>1,10,11,14,15,\*</sup>

<sup>1</sup>Department of Dermatology, University of Cologne, 50937 Cologne, Germany

<sup>2</sup>Department of Immunometabolism, Max Planck Institute of Epigenetics and Immunobiology, 79108 Freiburg im Breisgau, Germany

<sup>3</sup>Max Planck Institute for Metabolism Research, 50931 Cologne, Germany

<sup>4</sup>Helmholtz Institute for Metabolic, Obesity and Vascular Research (HI-MAG) of the Helmholtz Zentrum München at the University of Leipzig and University Hospital Leipzig, 04103 Leipzig, Germany

<sup>5</sup>Genomics & Immunoregulation, LIMES-Institute, University of Bonn, 53115 Bonn, Germany

<sup>6</sup>Platform for Single Cell Genomics and Epigenomics (PRECISE) at the German Center for Neurodegenerative Diseases and the University of Bonn, 53127 Bonn, Germany

<sup>7</sup>Institute for Biochemistry II, Center for Biochemistry, University of Cologne, 50931 Cologne, Germany

<sup>8</sup>Institute for Mitochondrial Diseases and Ageing, Medical Faculty, University of Cologne, 50931 Cologne, Germany

<sup>9</sup>Max Planck Institute for Biology of Ageing, 50931 Cologne, Germany

<sup>10</sup>Center for Molecular Medicine Cologne (CMMC), University of Cologne, 50931 Cologne, Germany

<sup>11</sup>Cologne Excellence Cluster on Cellular Stress Responses in Aging-Associated Diseases (CECAD), University of Cologne, 50674 Cologne, Germany

<sup>12</sup>Institute for Immunology, Medical Faculty, TU Dresden, 01307 Dresden, Germany

<sup>13</sup>Faculty of Biology, University of Freiburg, 79104 Freiburg im Breisgau, Germany

<sup>14</sup>Institute of Zoology, Developmental Biology Unit, University of Cologne, 50674 Cologne, Germany

<sup>15</sup>Lead contact

\*Correspondence: [sabine.eming@uni-koeln.de](mailto:sabine.eming@uni-koeln.de)

<https://doi.org/10.1016/j.cmet.2021.10.004>

## SUMMARY

Wound healing is a coordinated process that initially relies on pro-inflammatory macrophages, followed by a pro-resolution function of these cells. Changes in cellular metabolism likely dictate these distinct activities, but the nature of these changes has been unclear. Here, we profiled early- versus late-stage skin wound macrophages in mice at both the transcriptional and functional levels. We found that glycolytic metabolism in the early phase is not sufficient to ensure productive repair. Instead, by combining conditional disruption of the electron transport chain with deletion of mitochondrial aspartyl-tRNA synthetase, followed by single-cell sequencing analysis, we found that a subpopulation of early-stage wound macrophages are marked by mitochondrial ROS (mtROS) production and HIF1 $\alpha$  stabilization, which ultimately drives a pro-angiogenic program essential for timely healing. In contrast, late-phase, pro-resolving wound macrophages are marked by IL-4R $\alpha$ -mediated mitochondrial respiration and mitohormesis. Collectively, we identify changes in mitochondrial metabolism as a critical control mechanism for macrophage effector functions during wound healing.

## INTRODUCTION

Restoration of tissue integrity and homeostasis after injury is a fundamental biological process, which is required for the survival of all organisms. In most tissues, injury induces a highly dynamic cellular repair program that proceeds in sequential phases of antimicrobial defense (generally considered the pro-inflammatory phase), followed by tissue growth and differentiation (referred to as the pro-resolution phase) (Gurtner et al., 2008). Cells of the monocyte/macrophage lineage

(M $\Phi$ s) are an essential component of the body's innate ability to restore tissue function after injury (Eming et al., 2017; Murray and Wynn, 2011). Previously, we and others have shown that to ensure an optimal wound healing response, M $\Phi$ s need to rapidly adopt diverse activation states in response to their tissue-damaged microenvironment. Specifically, upon recruitment of circulating blood monocytes into the site of tissue injury, initially they need to acquire a type-1-activated pro-inflammatory and pro-angiogenic M $\Phi$  phenotype to support microbial defense, tissue vascularization, and



regenerative growth of the damaged tissue (Lucas et al., 2010; Mirza et al., 2009; Willenborg et al., 2012). Later, once the immediate danger has passed, the initial inflammatory phenotype of the MΦs shifts toward a type-2-activated resolution phenotype to promote scar formation and repair (Bosurgi et al., 2017; Gause et al., 2013; Knipper et al., 2015). However, the molecular signals required to coordinate the transition from pro-inflammatory clearance of injury-associated MΦs to pro-resolution signals that rebuild tissue architecture and restore homeostasis remain unresolved (reviewed in Eming et al., 2021).

Emerging evidence, as yet mostly generated *in vitro*, highlights that cellular metabolism is tightly linked to immune cell activation and function (O'Neill and Pearce, 2016; Rambold and Pearce, 2018; Zhang et al., 2019). Thereby, adaptation in immune cell metabolism leads not only to changes in energy metabolism (i.e., ATP production) but also to regulation of the activation phenotype of these cells via changes in gene expression (Sanin et al., 2018). Interestingly, a recent study of the human brain identified a relationship between a strong glycolytic signature in injury-associated MΦs during the acute phase of the myeloid response to intracerebral hemorrhage with positive outcome in the patient (Askenase et al., 2021). Yet, a direct *in vivo* causal link between tissue injury, metabolism, and distinct MΦ repair functions has yet to be established. Understanding and modulating the metabolic pathways in injury-associated MΦs could help to untangle the molecular basis that coordinates the functional diversity of wound MΦs, and this insight might provide a powerful approach to facilitate the regenerative capacity of tissues (reviewed in Eming et al., 2021).

To untangle the functional relationship between cellular metabolism and specific repair effector functions in injury-associated MΦs, we performed a comparative analysis of early- versus late-stage wound MΦs at both the transcriptional and functional levels. Our findings in bulk and single-cell RNA sequencing (scRNA-seq) analysis reveal that wound MΦs at different stages during the repair response commit to specific metabolic programs that are critical to support their stage-specific wound repair functions. Interestingly, in mice with myeloid-cell-specific disruption of the electron transport chain (ETC) (i.e., *Dars2*<sup>MKO</sup> mice), we found that early-phase wound MΦs require both glycolysis and repurposing of mitochondrial activity (namely, the generation of mtROS) to generate an appropriate early-stage, pro-inflammatory, and vascular response that ensures timely healing. In contrast, late-phase wound MΦs, which depend on IL-4Rα signaling to promote tissue repair, are engaged in oxidative phosphorylation (OXPHOS) but also display features of a so far unknown mitochondrial stress response regulation. Based on this data, we propose that in physiological repair but also in scenarios of perturbed mitochondrial activity as modeled in *Dars2*<sup>MKO</sup> mice, type-2 immune signals protect mitochondrial function by regulating and adjusting the mitochondrial stress response, which ultimately strengthens repair effector functions of late-stage wound MΦs. Together, our findings highlight individual metabolic characteristics as an additional regulatory dimension of diverse effector functions in wound MΦs. This new insight could lead to the identification of new pharmaceutical targets to facilitate the healthy repair of injured tissues.

## RESULTS

### Distinct metabolic profiles determine early- versus late-phase wound MΦs

To investigate the metabolic signature in wound MΦs (herein-after defined as CD45<sup>+</sup>CD11b<sup>+</sup>F4/80<sup>+</sup> cells) during the entire repair response, we used a model of full-thickness excisional skin injury to the back skin of C57BL/6 wild-type mice. We isolated injury-associated MΦs from wound tissue during the early inflammatory phase (4 days post-injury [dpi]) and in the late scar-forming phase (14 dpi), sorted them by flow cytometry, and subjected them to extracellular flux analysis (EFA). Changes in the oxygen consumption rate (OCR) and the basal extracellular acidification rate (ECAR, a measure of lactate production that reflects glycolysis rate) were determined. We found a higher basal respiration (before any treatment), ATP turnover (upon addition of ATP synthase inhibitor oligomycin), and spare respiratory capacity [difference between basal and maximal respiration upon addition of uncoupling agent carbonyl cyanide 4-(trifluoromethoxy) phenylhydrazone (FCCP)] in late-phase wound MΦs compared with early-phase wound MΦs (Figure 1A). In contrast, we found that early-phase wound MΦs had a significantly higher degree of glycolysis compared with late-stage MΦs based on basal ECAR values (Figure 1B). Consistent with higher OCR in late-phase wound MΦs, we found a higher mitochondrial mass in these cells compared with early-phase MΦs as shown by Mito-Tracker<sup>TM</sup> Green (MTG) fluorescent staining and flow cytometric analysis (Figure 1C). Taken together, we show that wound MΦs are characterized by phase-specific energetic metabolic profiles and that increased oxygen consumption in the late-phase of healing is due to increased mitochondrial OXPHOS and expansion of the mitochondrial network.

### Wound phase-specific metabolic pathways in MΦs are synchronized with distinct metabolic transcriptional profiles

We questioned whether wound MΦs induce the expression of specific gene sets to acquire their phase-specific metabolic profile. For this purpose, we compared the bulk transcriptome of early- versus late-phase wound MΦs by RNA-seq (Figure S1A). Unbiased principal component analysis (PCA) based on all identified 13,674 transcripts and hierarchical clustering (HC) based on the 1,000 most variable present genes ( $p \leq 0.05$ ) revealed profound transcriptional differences between early- and late-phase wound MΦs (Figures S1B and S1C). We determined differentially expressed genes (fold change  $\geq 2$ , adjusted  $p \leq 0.05$ ) between early- and late-phase wound MΦs by using a one-way ANOVA model and plotted the ratios against the adjusted  $p$  values in a volcano plot (Figure 1D). Expression of 446 and 480 genes was significantly higher in early- and late-phase wound MΦs compared with each other. Whereas we found higher expression of pro-inflammatory (*Nos2* and *Ptgs2*) and pro-angiogenic (*Vegfa*) genes in early-phase wound MΦs compared with the late-phase, the expression of prominent type 2 cytokine-induced genes (*Ccl22*, *Ear2*, *Irf4*, *Mgll*, *Mgl2*, *Mrc1*, and *Retnla*) was higher in late-phase wound MΦs than those in the early-phase. Interestingly, in parallel to these pro-inflammatory toward pro-resolution activation patterns during healing progression, we found specific enrichment of distinct

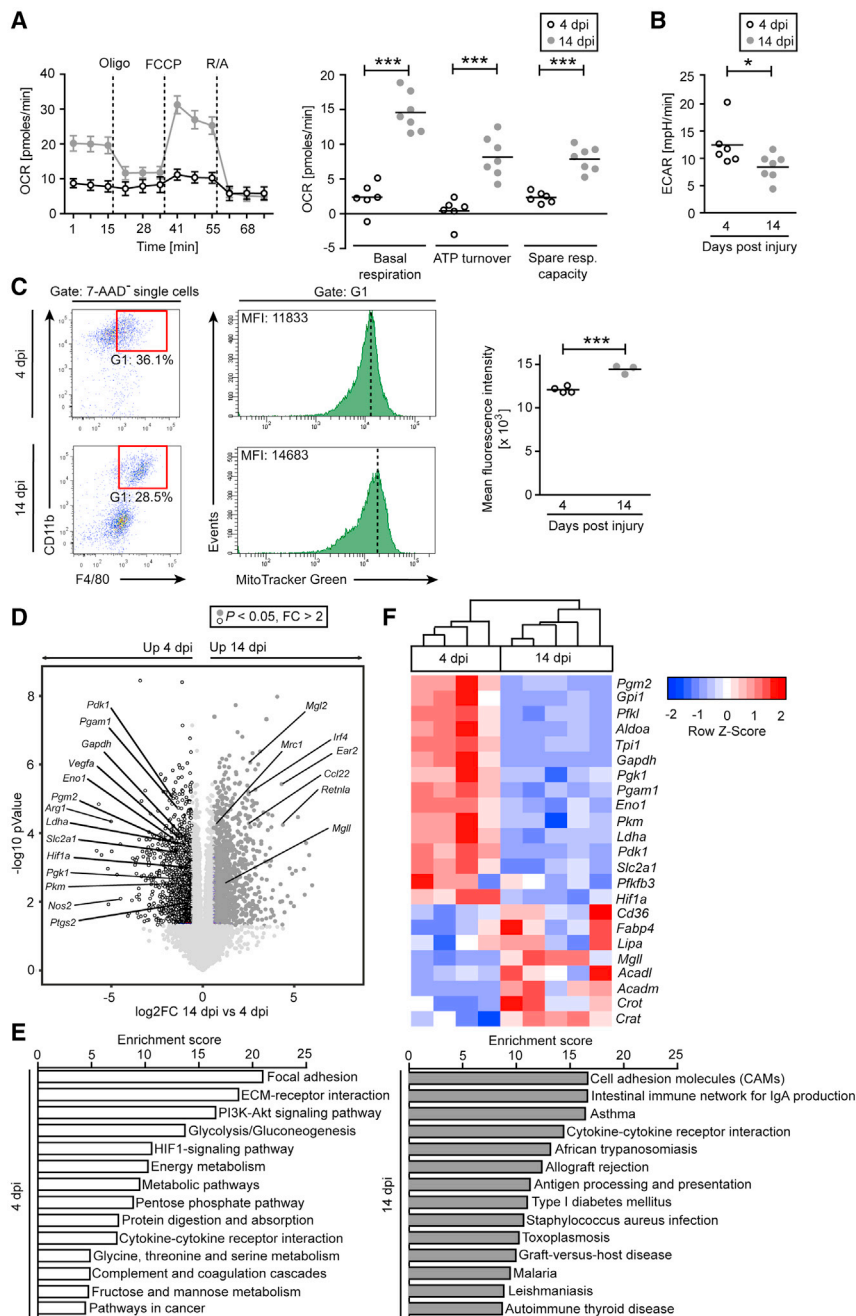


**Figure 1. Distinct metabolic profiles determine early- versus late-phase wound MΦs**

(A and B) EFA of OCR (A) and ECAR (B) in sorted wound MΦs isolated from wild-type mice at indicated time points. (A) Cells were sequentially treated with oligomycin (Oligo), FCCP, and rotenone/antimycin A (R/A) as indicated. n = 6 (4 dpi) and 7 (14 dpi) technical replicates of 1 biological replicate. Left panel, the mean value ± SEM is represented.

(C) Representative flow cytometry plots (n = 4 at 4 dpi and 3 at 14 dpi in total) of mitochondrial mass analysis by MTG fluorescent staining in wild-type wound MΦs. 7-AAD<sup>−</sup>CD11b<sup>+</sup>F4/80<sup>+</sup> cells were gated (G1), and the mean fluorescence intensity (MFI) was analyzed. Dashed line indicates peak of the fluorescent signal. One technical replicate of 4 (4 dpi) and 3 (14 dpi) biological replicates.

(D–F) RNA-seq analysis in sorted wound MΦs. One technical replicate of 4 biological replicates at 4 dpi and 5 at 14 dpi. (D) Volcano plot of all identified genes. FC, fold change. (E) Pathway enrichment analysis. (F) HC showing the z-transformed expression values of indicated genes.

(A–C) \*p < 0.05, \*\*\*p < 0.001 by Student's unpaired two-tailed t test.

(Figure 1E). Moreover, early-phase wound MΦs showed enrichment of specific mitochondrial processes including “heme metabolic process,” “citrate metabolic process,” and “succinate metabolic process,” as revealed by gene ontology enrichment (GOE) analysis and based on MitoCarta 3.0 datasets (Figure S1D). In contrast, late-phase wound MΦs were enriched in type-2-cytokine-induced pathways such as “asthma” and showed higher expression of genes involved in fat uptake (*Cd36*) and catabolic metabolism, such as lipolysis (*Fabp4*, *Lipa*, and *Mgl1*) and fatty acid oxidation (FAO; *Acadl*, *Acadm*, *Crot*, and *Crat*) compared with the early-phase (Figures 1E and 1F). Moreover, late-phase wound MΦs were enriched in mitochondrial processes such as “carnitine metabolic process,” “tRNA aminoacylation for mitochondrial protein translation,” “ATP transport,” and “mitochondrial DNA replication,” supporting our finding of increased oxidative metabolism and mitochondrial biogenesis (Figure S1D).

To corroborate the transcriptional differences identified in the RNA-seq analysis and to elaborate on the transcriptional profile of the early inflammatory response, we subjected sorted wound MΦs at 2, 4, and 14 dpi to quantitative real-time PCR analysis (qRT-PCR) and normalized the data to gene expression in sorted SSC<sup>low</sup>CD11b<sup>+</sup>CD115<sup>+</sup> blood monocytes. We found markedly higher expression of glycolytic genes and *Hif1a* in wound MΦs at 2 dpi compared with blood monocytes, while the expression of these genes declined during healing progression (Figure S1E). In contrast, lipases and FAO-related genes showed a steady

metabolic pathways. In line with increased ECAR (Figure 1B), early-phase wound MΦs showed enrichment of the pathways “glycolysis/gluconeogenesis” and “HIF-1 signaling,” a critical inducer of glycolytic genes (Tannahill et al., 2013) (Figure 1E). Specifically, wound MΦs at 4 dpi expressed significantly higher levels of the facilitative glucose transporter *Slc2a1*, enzymes of the glycolytic pathway, *Pfkfb3* (known to potentiate the glycolytic flux; Rodríguez-Prados et al., 2010), and *Hif1a* compared with wound MΦs at versus 14 dpi (Figure 1F). Besides glycolysis, we also found a signature of anabolic metabolism in early-phase wound MΦs, as revealed by enrichment of “PI3K-Akt signaling pathway” and “pentose phosphate pathway” (PPP)



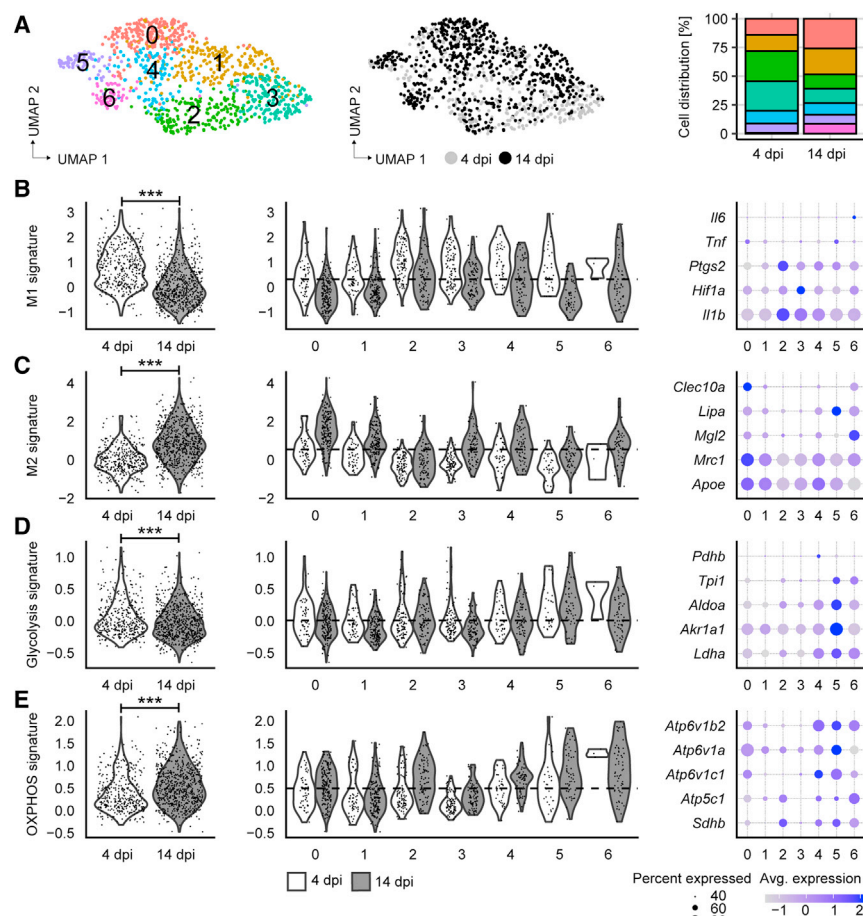


**Figure 2. Wound MΦs display striking heterogeneity across activation patterns and metabolic signatures**

(A–E) Single-cell RNA-seq analysis of wild-type wound MΦs isolated at 4 and 14 dpi. (A) UMAP highlights identified clusters. (B–E) Left and mid panels, violin plots showing M1, M2, glycolysis, and OXPHOS signatures at indicated time points and in each cluster. Right panels, dot plots showing the most variable genes used in the score calculations. \*\*\* $p < 0.001$  by two-factor ANOVA with Tukey’s “honest significant difference” method.

score, particular at 4 dpi (Figures 2C–2E, mid and right panel). Taken together, scRNA-seq analysis supports our bulk characterization of MΦ populations, corroborating a shift from M1-like/glycolytic toward M2-like/oxidative MΦs as the wound heals. Of particular interest, the analysis highlights a vast heterogeneity among wound MΦs with regard to activation phenotypes and metabolic signatures. These findings uncover different metabolic regulation occurring in parallel across early- and late-stage MΦ populations.

### DARS2 controls mitochondrial respiratory chain function and BMDM activation

Mitochondria play a central role in metabolic rewiring during MΦ polarization.

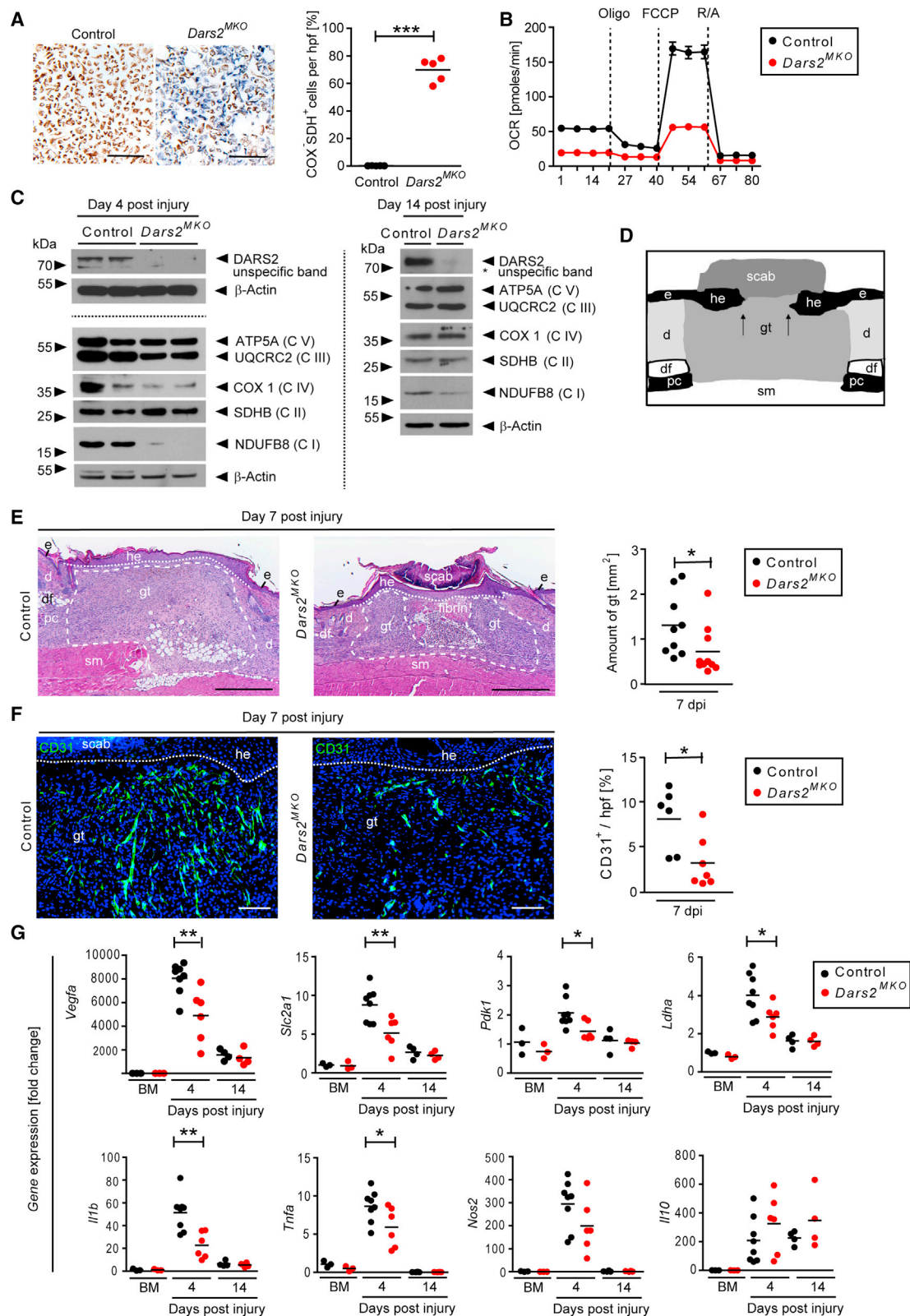
increase after injury until the late-phase of the repair response (Figure S1E). Collectively, our findings reveal that phase-specific metabolic functions of wound MΦs are paralleled by the induction of distinct and corresponding gene expression signatures.

### Wound MΦs display strong heterogeneity across activation patterns and metabolic signatures

To address the question of heterogeneity across activation signatures and metabolic programs in wound MΦs, we performed single-cell RNA sequencing (scRNA-seq) analysis of early- and late-stage wound MΦs. Interestingly, scRNA-seq analysis highlighted strong heterogeneity in MΦ populations over the time course of the wound healing response. MΦs clustered in seven populations as shown by uniform manifold approximation and projection (UMAP) (Figure 2A, left panel). Early-stage wound MΦs clustered predominantly in clusters 2 and 3, while late-stage wound MΦs were found predominantly in clusters 0, 1, and 6 (Figure 2A, mid and right panel). Consistent with bulk RNA analysis, 4 and 14 dpi wound MΦs were each significantly enriched in M1-like and glycolytic gene signatures, or M2-like and OXPHOS gene signatures, respectively, shown here as cumulative gene expression scores (Figures 2B–2E, left panels). Interestingly, we found unexpected heterogeneity among clusters across activation patterns and metabolic signatures. For example, whereas cluster 6 only appeared at 14 dpi and was characterized by a strong M2-like, glycolytic and OXPHOS signature, cluster 3 had the lowest OXPHOS

This has been intensively studied, particularly in different *in vitro* scenarios (Vats et al., 2006; Mills et al., 2016; Sanin et al., 2018). However, the mechanistic details of which mitochondrial signals might regulate the pro-inflammatory toward pro-resolution behavior in injury-associated MΦs are elusive. To address this question, we established a genetic mouse model that conditionally disrupts the mitochondrial respiratory chain (MRC) specifically in myeloid cells by *Dars2* gene deletion (*Dars2*<sup>loxP/loxP</sup>*Lyz2-cre* mice, and *Dars2*<sup>MKO</sup>) (Figure S2A) (Clayson et al., 1999; Dogan et al., 2014). *Dars2* encodes mitochondrial aspartyl-tRNA synthetase 2, which is critical for protein synthesis inside mitochondria. *Dars2*<sup>MKO</sup> mice were born at the expected Mendelian ratios, developed normally and did not show major spontaneous phenotypes in specific-pathogen-free (SPF) conditions. We confirmed efficient *Lyz2-cre*-mediated *Dars2* gene deletion in bone-marrow-derived macrophages (BMDMs) isolated from *Dars2*<sup>MKO</sup> and control mice (Figures S2A–S2D). Western blot analysis of whole cell lysates of *Dars2*-deficient BMDMs after 12 days of culture showed lower levels of MRC complex I (C I) subunit NDUFB8 and MRC complex IV (C IV) subunit COX4 compared with controls (Figure S2D), and those culture conditions were used throughout the study. Of note, absolute cell numbers and cell viability were similar in control and *Dars2*-deficient BMDMs (Figures S2E and S2F).

Lower levels of MRC subunits in *Dars2*-deficient BMDMs resulted in loss of MRC complexes and their activity, as confirmed



(legend continued on next page)

by enzyme histochemical double staining for COX (cytochrome c oxidase, C IV) and SDH (succinate dehydrogenase, MRC complex II, C II) activities. Whereas control BMDMs showed uniform COX activity (brown staining), 69.9%  $\pm$  8.7% of BMDMs isolated from *Dars2*<sup>MKO</sup> mice displayed MRC deficiency characterized by loss of COX activity (blue staining is due to SDH activity) (Figure 3A). Further, we detected significantly lower basal respiration, ATP turnover, and spare respiratory capacity in *Dars2*-deficient BMDMs versus control cells by oxygen consumption measurements (Figure 3B). The basal glycolysis rate and the glycolytic capacity were not significantly altered in *Dars2*-deficient BMDMs, indicating that in steady-state conditions these cells do not compensate for the impaired mitochondrial respiration by increasing glycolysis (Figure S2G).

We then asked whether perturbed mitochondrial protein synthesis in *Dars2*-deficient BMDMs impacts cellular activation. Lipopolysaccharide (LPS) + IFN- $\gamma$  treatment of BMDMs [M(LPS + IFN- $\gamma$ )] significantly induced expression of pro-inflammatory mediators (*Il1b*, *Il6* and *Tnfa*) in controls, whereas the response was blunted in *Dars2*-deficient BMDMs (Figure S2H). Notably, we found significantly higher expression of *Il10* in *Dars2*-deficient M(LPS + IFN- $\gamma$ ) compared with control M(LPS + IFN- $\gamma$ ), demonstrating a switch to an overall anti-inflammatory phenotype (Figure S2H). IL-4 + IL-13 treatment of BMDMs [M(IL-4 + IL-13)] induced expression of *Retnla*, *Arg1*, and *Chil3* in control BMDMs, whereas expression of *Retnla* and *Arg1* was attenuated in IL-4 + IL-13-treated *Dars2*-deficient BMDMs compared with treated controls (Figure S2H). Of note, although transcriptional levels were reduced at statistically significant levels in *Dars2*-deficient BMDMs; cells maintained a considerable residual transcriptional activity compared with unstimulated cells. Nevertheless, these findings demonstrate *in vitro* a clear causal link between *Dars2* expression (and thus likely mitochondrial protein synthesis) and activation of both pro-inflammatory and pro-resolution M $\Phi$  phenotypes.

### Myeloid-cell-specific MRC function is essential for angiogenesis during skin repair

Next, we set out to analyze whether myeloid-cell-specific MRC deficiency impacts *in vivo* repair functions of wound M $\Phi$ s and inflicted excision skin wounds on the back of *Dars2*<sup>MKO</sup> and control mice. First, we confirmed efficient *Lyz2-cre*-mediated *Dars2* gene deletion *in vivo* in sorted wound M $\Phi$ s and SSC<sup>low</sup>CD115<sup>+</sup>CD11b<sup>+</sup> blood monocytes from *Dars2*<sup>MKO</sup> mice compared with controls at all stages of repair (Figure S3A). Western blot analysis in wound M $\Phi$ s at 4 and 14 dpi revealed a significant reduction of

NDUFB8 (C I) and a moderate reduction of UQCRC2 (MRC complex III, C III) and COX1 (C IV) in *Dars2*-deficient wound M $\Phi$ s compared with control cells, thereby demonstrating MRC deficiency (Figure 3C). Notably, at 14 dpi, we found that the levels of C III and C IV subunits in *Dars2*-deficient wound M $\Phi$ s appeared less attenuated and were almost comparable to controls (Figure 3C). Importantly, DARS2 was absent in day-14 wound M $\Phi$ s (Figure 3C). In order to further rule out a possible replacement of mutants by wild-type cells, we carried out a fate-mapping experiment in which we traced the recruitment of monocytes in different phases of wound healing. We injected red fluorescent monocytes (tdRFP<sup>+</sup>) at 2 or 12 dpi intravenously into wild-type mice and analyzed wound M $\Phi$ s by flow cytometry at 4 and 14 dpi (Figures S3B and S3C). As expected, adoptively transferred monocytes robustly infiltrated the wound between 2 and 4 dpi, and these cells partially persisted until 14 dpi. By contrast, between 12 and 14 dpi, when the epidermis is closed, significantly less monocytes were recruited into the wound tissue compared with the early-phase of healing (Figures S3B and S3C). Together, our findings argue against a replacement of *Dars2*-deficient wound M $\Phi$ s by wild-type cells and suggest that in the late, type-2-skewed wound environment compensatory mechanisms might be activated in *Dars2*<sup>MKO</sup> mice to overcome myeloid-cell-restricted MRC deficiency.

We then analyzed whether the wound healing response and the capability to restore tissue architecture might be affected in *Dars2*<sup>MKO</sup> mice. Interestingly, histomorphological analyses revealed a severe delay in wound closure dynamics in mutants versus control mice, evident by several important features: significant reduction of granulation tissue (Figure 3E), profoundly prolonged persistence of provisional extracellular wound matrix such as fibrin, even up to 7 dpi (Figures 3E and S3D), delayed scab shedding (Figure 3E), and significantly reduced wound vascularization in early wound tissue (Figure 3F). These alterations are consistent with major and established deficits during the early- and mid-phase of the repair response (Gurtner et al., 2008; Hunt et al., 2007; Knipper et al., 2015; Lucas et al., 2010; Mirza et al., 2009; Willenborg et al., 2012). Numbers of wound M $\Phi$ s at 4 and 14 dpi were comparable in control and *Dars2*<sup>MKO</sup> mice, indicating that neither recruitment of blood monocytes into the site of injury nor cell viability at the wound site were affected by *Dars2* deficiency (Figure S3E).

HIF1 $\alpha$ -mediated *Vegfa* expression in myeloid cells is a critical regulator of vascular sprouting in skin repair (Willenborg et al., 2012). Notably, *Dars2*-deficient early-phase wound M $\Phi$ s expressed significantly lower levels of known important HIF1 $\alpha$  repair

(B) EFA of OCR in BMDMs. Cells were sequentially treated with oligomycin (Oligo), FCCP, and rotenone/antimycin A (R/A) as indicated. Eight technical replicates of 1 biological replicate per genotype. The mean value  $\pm$  SEM is represented.

(C) Western blot analysis of DARS2 and MRC complex subunits in sorted wound M $\Phi$ s at indicated time points. Dashed lines indicate the use of different gels. One technical replicate of 2 (4 dpi) and 1 (14 dpi) biological replicates per genotype.

(D) Schematic illustrating skin wound histology at around 4 dpi. d, dermis; df, dermal fat tissue; e, epidermis; gt, granulation tissue; he, hyperproliferative epithelium; pc, panniculus carnosus; sm, skeletal muscle. Arrows indicate the tips of the epithelial tongues.

(E) Representative H&E-stained wound sections at 7 dpi (n = 9 control wounds, 10 *Dars2*<sup>MKO</sup> wounds in total) and quantitative analysis of granulation tissue (gt). Scale bar, 500  $\mu$ m. One technical replicate of 9 (control) and 10 (*Dars2*<sup>MKO</sup>) biological replicates.

(F) Representative CD31 immunostainings at 7 dpi (n = 6 control wounds, 7 *Dars2*<sup>MKO</sup> wounds in total) and quantification of CD31<sup>+</sup> area per high power field (hpf). Nuclear staining: DAPI. Scale bar, 100  $\mu$ m. 1 technical replicate of 6 (control) and 7 (*Dars2*<sup>MKO</sup>) biological replicates.

(G) qRT-PCR analysis in sorted wound M $\Phi$ s normalized to blood monocytes. One technical replicate of n = 3 biological replicates per group for BM, 8 controls at 4 dpi, 6 *Dars2*<sup>MKO</sup> at 4 dpi, 4 per group at 14 dpi. BM, blood monocytes.

\*p < 0.05, \*\*p < 0.01, \*\*\*p < 0.001 by Student's unpaired two-tailed t test (A, and E–G).



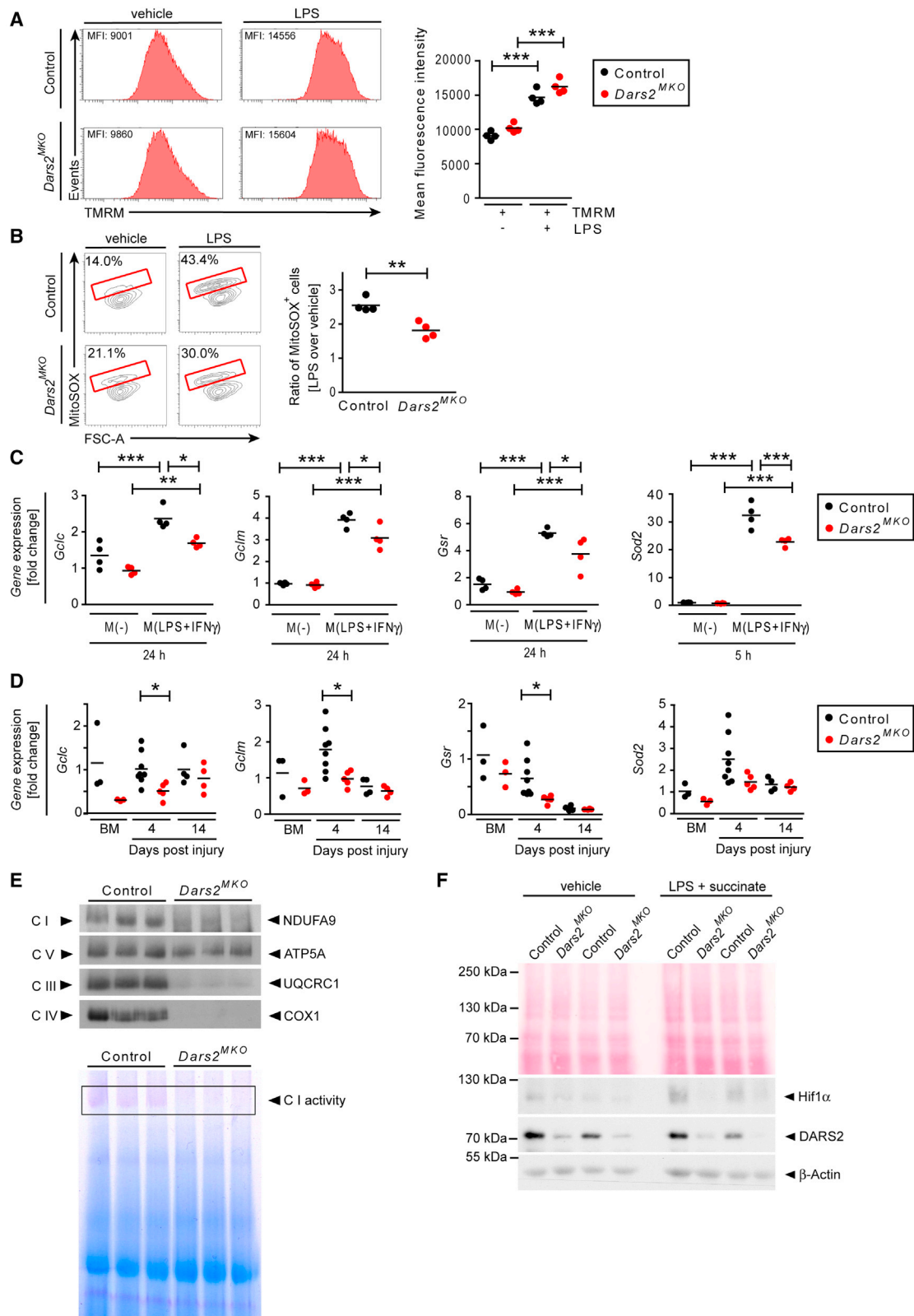


**Figure 4. Pro-angiogenic MΦs require repurposing of MRC function to achieve sufficient levels of active HIF1α**

(A) Representative flow cytometry plots (n = 4 per group in total) of MMP analysis in BMDMs stimulated with LPS (100 ng/mL) or vehicle for 48 h by TMRM staining (100 nM). Single cells were gated and the TMRM MFI was determined. Four technical replicates of 1 biological replicate per group.

(legend continued on next page)



target genes, including *Vegfa*, glycolytic and pro-inflammatory genes, whereas anti-inflammatory *Il10* showed a trend toward higher expression at 4 and 14 dpi compared with controls (Figure 3G). Taken together, these findings show that in early-phase wound MΦs, proper MRC function is required to generate an appropriate HIF1 $\alpha$ -mediated pro-angiogenic and early inflammatory wound response that ensures timely healing. Intriguingly, our findings *in vivo* suggest that a glycolytic signature is not sufficient to support an effective pro-angiogenic response required for a productive repair response.

### Pro-angiogenic wound MΦs require repurposing of MRC function to achieve sufficient levels of active HIF1 $\alpha$

Next, we set out to explore the mechanistic link between myeloid-cell-specific *Dars2*-deficiency and poor wound vascularization. Previous findings showed that in their LPS response BMDMs require repurposing of MRC function from ATP production toward mtROS production at C I upon succinate oxidation for HIF-mediated IL-1 $\beta$  synthesis (Mills et al., 2016). In addition, mtROS generated from C III in response to LPS + IFN- $\gamma$  are required for the inflammatory phenotype of BMDMs (Cameron et al., 2019). Whether mtROS production in injury-associated MΦs is critical for HIF1 $\alpha$ -mediated tissue vascularization is elusive. Interestingly, our RNA-seq analysis of wound MΦs in healthy mice revealed higher expression of genes involved in ROS detoxification and succinate metabolism in early- versus late-phase wound MΦs, which strongly suggests higher ROS production in early-phase wound MΦs (Figures S4A and S4B). Due to decreased levels of C I and C III in *Dars2*-deficient MΦs, we hypothesized that decreased mtROS production in mutant wound MΦs may contribute to impaired HIF1 $\alpha$  stabilization.

To test this hypothesis, we first analyzed the mitochondrial membrane potential (MMP) in control and *Dars2*-deficient BMDMs. An increased MMP can be a critical regulator of mtROS production from both C I and C III (Murphy, 2009). Tetramethylrhodamine methyl ester (TMRM) staining and subsequent flow cytometry showed similar MMP in control and *Dars2*-deficient BMDMs in vehicle-treated conditions (Figure 4A). Further, LPS treatment resulted in a significant increase in the MMP in both control and *Dars2*-deficient MΦs (Figure 4A). This finding shows that *Dars2*-deficient BMDMs are able to adapt their MMP under inflammatory conditions. Next, we assessed mtROS production by staining cells with the MitoSOX<sup>TM</sup> Red mitochondrial superoxide indicator. Stimulation of control BMDMs with LPS resulted in a  $2.6 \pm 0.2$ -fold increase in MitoSOX<sup>+</sup> cells over vehicle-treated cells, whereas the LPS-induced mtROS production in *Dars2*-deficient cells was significantly lower ( $1.8 \pm 0.2$ -fold) (Figure 4B). To

further substantiate our findings of reduced mtROS production in *Dars2*-deficient MΦs, we also analyzed the expression of genes critical for ROS detoxification. Notably, expression of *Gclc*, *Gclm*, *Gsr*, and *Sod2* was significantly lower in *Dars2*-deficient *in vitro* LPS + IFN- $\gamma$ -treated BMDMs and *Dars2*-deficient *in vivo* early-phase wound MΦs compared with controls (Figures 4C and 4D).

We further corroborated impaired assembly and activity of MRC complexes by blue native polyacrylamide gel electrophoresis (BN-PAGE) of individual MRC complexes in mitochondria isolated from BMDMs. The analysis revealed severely impaired assembly of C I, C III and C IV, and lower C I activity in *Dars2*-deficient versus control cells (Figure 4E). Loss of C I activity and C III assembly strongly correlated with the inability of *Dars2*-deficient BMDMs to stabilize HIF1 $\alpha$  upon LPS + succinate treatment (Figure 4F). In summary, our findings provide evidence that *Dars2*-deficient MΦs have lost their ability to repurpose their mitochondria, resulting in impaired mtROS-regulated HIF1 $\alpha$  stabilization and impaired induction of a pro-inflammatory and pro-angiogenic MΦ phenotype, critical for timely angiogenesis and a productive early repair response.

### A defined pro-angiogenic subpopulation of early-phase wound MΦs shows features of mitochondrial repurposing

To solidify *in vivo* evidence for mitochondrial repurposing in wound MΦs in the early-phase of healing, we extended our scRNA-seq analysis. First, we set out to identify pro-angiogenic MΦ populations based on calculating an angiogenesis score (Corliss et al., 2016). As expected, the angiogenesis score was significantly enriched in wound MΦs at 4 versus 14 dpi (Figure 5A, left panel). Analysis of the individual clusters at 4 dpi revealed heterogeneity in the angiogenic potential across the different clusters with cluster 3 being among the highest for the angiogenesis score (Figure 5A, mid and right panel). Interestingly, the angiogenesis score correlated negatively with the OXPHOS score, clearly indicating that angiogenic wound MΦs do not rely on OXPHOS (Figure 5B). As a cluster which repurposes mitochondria should be high in glycolysis and low in OXPHOS, we calculated a glycolysis:OXPHOS gene expression ratio. Interestingly, we identified cluster 3 as the cluster with the highest glycolysis:OXPHOS ratio (Figure 5C). We next analyzed the enrichment of genes associated with mtROS production, inflammation, and angiogenesis in the individual clusters. At 4 dpi the genes *Il1b*, *Vegfa*, *Hif1a*, *Ldha*, and *Slc2a1* as well as the ROS-detoxifying genes *Gclc*, *Gclm*, *Gsr*, *Sod2*, and *Nfe2l2* were mainly enriched in the clusters 0, 2, 3, and 5 (Figure 5D). Notably, the gene *Idh1* (encoding isocitrate dehydrogenase) was downregulated in cluster 3 while *Acod1* (encoding *cis*-aconitate decarboxylase) was enriched, which is a

(B) Representative flow cytometry plots ( $n = 4$  per group in total) of mtROS analysis in BMDMs stimulated with LPS (200 ng/mL) or vehicle for 2 h by MitoSOX (2.5  $\mu$ M) staining. Single cells were gated, the proportion of MitoSOX<sup>+</sup> cells was determined, and the ratio of MitoSOX<sup>+</sup> cells was calculated as indicated. One technical replicate of 4 biological replicates per group.

(C) qRT-PCR analysis in BMDMs stimulated with LPS (50 ng/mL) and IFN- $\gamma$  (50 ng/mL) or vehicle for 5 h one technical replicate of  $n = 4$  biological replicates per group.

(D) qRT-PCR analysis in sorted wound MΦs normalized to blood monocytes. One technical replicate of  $n = 3$  biological replicates per group for BM, 8 controls at 4 dpi, 5 *Dars2*<sup>MDKO</sup> at 4 dpi, 4 per group at 14 dpi.

(E) Upper panel, BN-PAGE and subsequent Western blot analysis of OXPHOS complexes in mitochondria isolated from BMDMs. Antibodies against individual OXPHOS subunits were used. Lower panel, in-gel activity of C I performed after BN-PAGE. One technical replicate of  $n = 3$  biological replicates per genotype.

(F) Western blot analysis of indicated targets in BMDM. Cells were pretreated with 5 mM succinate in growth medium for 3 h, followed by stimulation with LPS (100 ng/mL) for 48 h 1 technical replicate of  $n = 2$  biological replicates per group.

\* $p < 0.05$ , \*\* $p < 0.01$ , \*\*\* $p < 0.001$  by one-way ANOVA with Tukey's multiple comparison test (A and C) or Student's unpaired two-tailed t test (B and D).

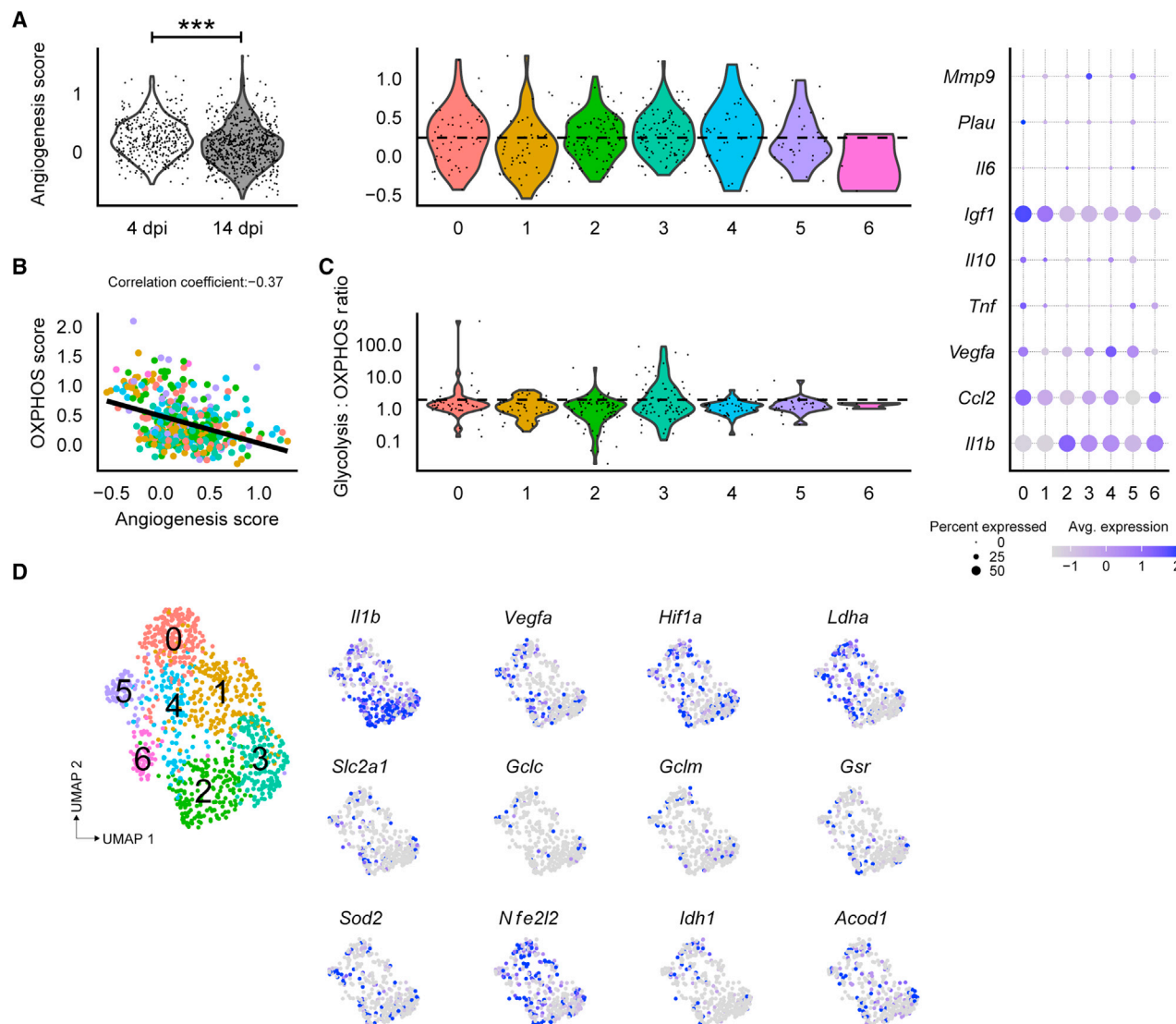


**Figure 5. A defined pro-angiogenic subpopulation of early-phase wound MΦs shows features of mitochondrial repurposing**

(A–D) Single-cell RNA-seq analysis of wild-type wound MΦs isolated at 4 and 14 dpi.

(A) Left and mid panels, violin plots showing the angiogenesis score at indicated time points and in individual clusters at 4 dpi. Right panel, dot plot showing the most variable genes used in the angiogenesis score calculation. \*\*\* $p < 0.001$  by two-factor ANOVA with Tukey's "honest significant difference" method.

(B) Correlation between angiogenesis and OXPHOS score at 4 dpi.

(C) Violin plot showing the glycolysis score:OXPHOS score ratio in individual clusters at 4 dpi.

(D) Distribution of indicated genes across the individual clusters at 4 dpi.

hallmark of M1-like MΦs and reflects a broken TCA cycle (Jha et al., 2015) (Figure 5D). Taken together, we conclude that cluster 3 likely represents a wound MΦ population that repurposes mitochondria to produce mtROS, and that is critical for effective wound vascularization as it shows hallmarks of a broken TCA cycle and has a high angiogenic potential and the highest glycolysis:OXPHOS ratio among the identified clusters.

### Type-2 immune signals support MRC function in *Dars2*-deficient MΦs

Despite efficient *Dars2* gene deletion, individual MRC subunits in the late-phase wound MΦs in mutant mice appeared to be

stabilized as their levels did not differ notably from the early-phase wound MΦs (Figure 3C, right panel). Surprisingly, the analysis of M2-like gene signature revealed comparable induction of hallmark type 2 mediators, such as *Retnla*, *Chil3*, and *Mrc1*, in both control and *Dars2*-deficient late-phase wound MΦs (Figure 6A). These findings were unexpected in light of the *in vitro* attenuated expression of IL-4 + IL-13-induced genes in *Dars2*-deficient BMDMs (Figure S2H). Hence, these findings indicate that in late-phase *Dars2*-deficient wound MΦs *in vivo* compensatory mechanisms are activated to protect mitochondrial function, ultimately ameliorating the activation defect of *Dars2*-deficient MΦ in the wound environment.

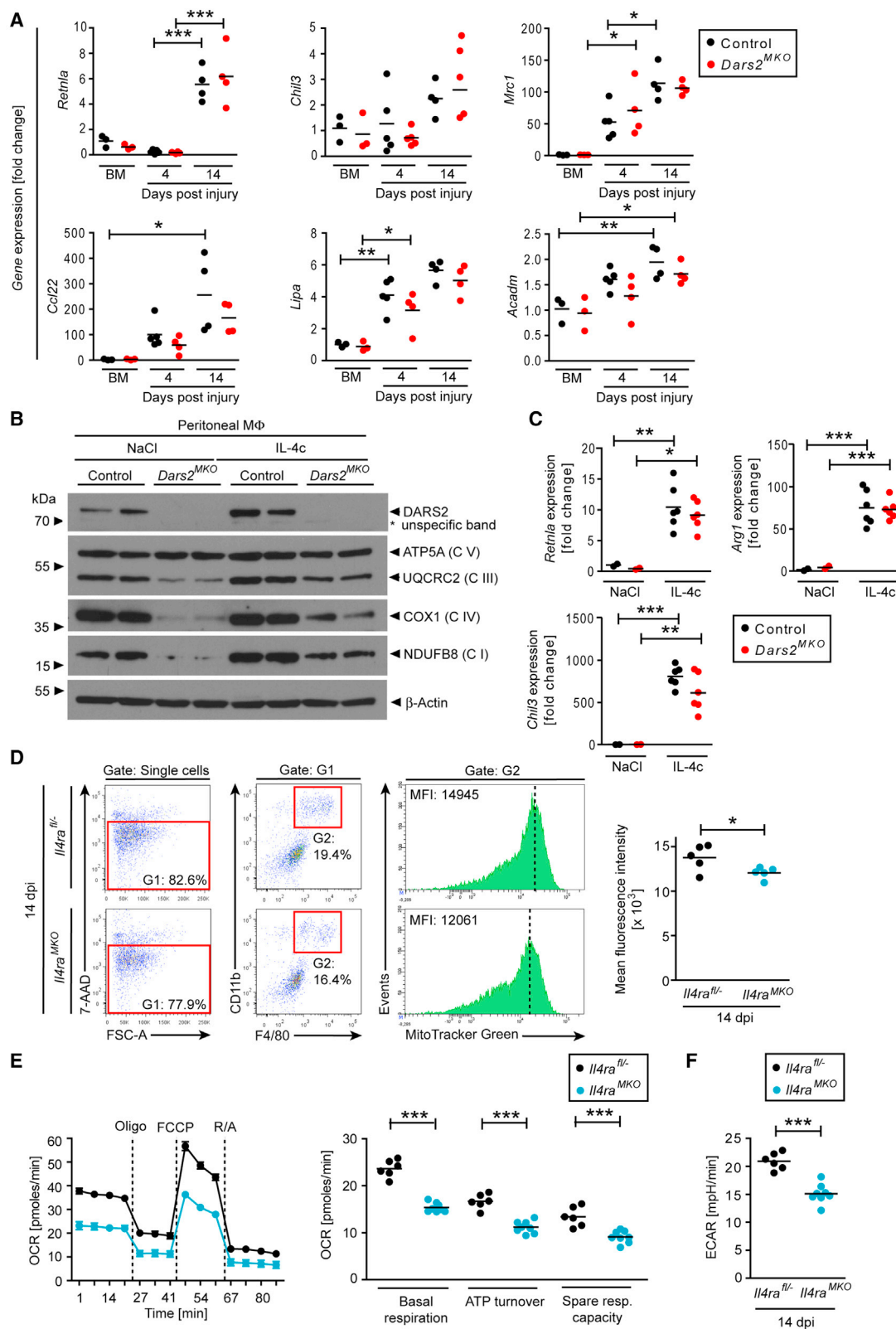


**Figure 6. Type-2 immune signals support MRC function in *Dars2*-deficient MΦs**

(A) qRT-PCR analysis in sorted wound MΦs normalized to blood monocytes. One technical replicate of  $n = 3$  biological replicates per group for BM, 5 per group at 4 dpi, 4 per group at 14 dpi. BM, blood monocytes.

(legend continued on next page)

To further corroborate the hypothesis that *in vivo* type 2 cytokines might stabilize MRC levels and promote MRC function in *Dars2*-deficient MΦ, we investigated MΦ function in a different, well established *in vivo* experimental model of type-2 immune stimulation (Jenkins et al., 2011). We challenged control and *Dars2*<sup>MKO</sup> mice with intraperitoneal injections of IL-4c (complex of IL-4 and anti-IL-4 antibody), which induces local MΦ proliferation and type-2 activation (Jenkins et al., 2011). IL-4c treatment of control mice resulted in an increase of MΦ numbers, while this response was attenuated in IL-4c-treated *Dars2*<sup>MKO</sup> mice (Figure S5A). This is notable because it shows that *in vivo* the IL-4-induced proliferation of tissue-resident MΦ in the peritoneum requires stable MRC complexes. Western blot analysis in sorted peritoneal MΦs revealed lower protein levels of NDUFB8, UQCRC2, COX1 in NaCl-treated *Dars2*-deficient cells when compared with NaCl-treated controls (Figure 6B). Notably, the abundance of these OXPHOS subunits was significantly higher in MΦs isolated from IL-4c-treated versus NaCl-treated *Dars2*<sup>MKO</sup> mice, corroborating the hypothesis of a type-2-mediated compensatory response (Figure 6B). Consistent with this observation, we found comparable expression of *Retnla*, *Arg1*, and *Chil3* in peritoneal MΦs sorted from IL-4c-treated control and *Dars2*<sup>MKO</sup> mice (Figure 6C). Taken together, our findings derived from two different experimental *in vivo* models suggest that type-2 immune signals support MRC stabilization and function in *Dars2*-deficient MΦs.

To further investigate this hypothesis, we first aimed to demonstrate that OXPHOS in late-stage wound MΦs is indeed regulated by IL-4Rα signaling. First, we analyzed the mitochondrial mass in wild-type BMDMs stimulated with IL-4 + IL-13 upon MTG staining followed by flow cytometry. We detected a significantly higher mitochondrial mass in IL-4 + IL-13-stimulated BMDMs when compared with vehicle-treated control cells (increased by 30.1% ± 15.0%), confirming type-2-cytokine-induced mitochondrial biogenesis (Figure S5B) (Vats et al., 2006). Next, we analyzed wound MΦs at 14 dpi isolated from myeloid-cell-restricted IL-4Rα-deficient (*Il4ra*<sup>fl/-</sup>-*Lyz2-cre*, *Il4ra*<sup>MKO</sup>) and control mice (*Il4ra*<sup>fl/-</sup>) using MTG staining coupled with flow cytometry. Notably, the mitochondrial mass was significantly lower (lowered to 87.6% ± 4.4% of controls) in IL-4Rα-deficient wound MΦs compared with controls, thereby supporting the notion that mitochondrial biogenesis in late-phase wound MΦs depends on IL-4Rα signaling (Figure 6D). We next investigated whether lower mitochondrial biogenesis in IL-4Rα-deficient wound MΦs leads to attenuated mitochondrial respiration. Analysis of the OCRs in sorted wound MΦs at 14 dpi revealed that basal respiration, ATP turnover, and spare respiratory capacity were significantly lower in late-phase IL-4Rα-deficient

MΦs compared with control cells (Figure 6E). In addition, the glycolysis rate, as measured by basal ECAR, was significantly attenuated in late-phase wound MΦs isolated from *Il4ra*<sup>MKO</sup> mice compared with late-phase wound MΦs isolated from control mice (Figure 6F). This finding is in line with previous *in vitro* and *in vivo* studies showing that IL-4 not only stimulates OXPHOS but also glucose uptake and metabolism in MΦs (Huang et al., 2016; Vats et al., 2006). Taken together, our findings show that type-2 cytokine signaling via IL-4Rα in late-phase wound MΦs is critical to induce mitochondrial biogenesis and OXPHOS. Notably, on a *Dars2*-deficient background mitochondrial function in MΦs is partially rescued by type-2 cytokines.

### Type 2 immune signals modulate mitochondrial stress responses and promote mitohormesis in wound MΦs

To untangle potential mechanisms as to how type 2 signals protect mitochondrial function, particularly in *Dars2*-deficient MΦs, we stimulated BMDMs isolated from control and *Dars2*<sup>MKO</sup> mice with IL-4 + IL-13 for 48 h and analyzed levels of MRC subunits. Consistent with impaired assembly levels of MRC complexes in mitochondrial isolates (Figure 4E), we found lower protein levels of MRC subunits NDUFB8, UQCRC2, and COX1 in whole cell lysates of *Dars2*-deficient BMDMs compared with controls (Figure 7A). Notably, while IL-4 + IL-13 stimulation did not have notable effects on MRC protein levels in control cells, we detected a stabilization of MRC subunits NDUFB8, UQCRC2, COX1, and ATP5A in stimulated versus unstimulated *Dars2*-deficient MΦs (Figure 7A). Stabilization of MRC subunits *in vitro* is consistent with our *in vivo* findings in *Dars2*-deficient MΦs in late-stage skin repair (Figure 3C) or IL-4c-stimulated peritonitis (Figure 6B). Notably, RNA-seq analysis of *in vitro* stimulated BMDMs revealed strong transcriptional changes induced by IL-4 + IL-13 in control and *Dars2*-deficient BMDMs and modest transcriptional changes induced by *Dars2* deficiency, as shown by PCA analysis and heatmap clustering (Figures S6A and S6B).

In non-immune cells it is well established that MRC deficiency, also caused by DARS2 deficiency, induces compensatory stress responses, in particular mitochondrial integrated stress response (mitoISR) characterized by the ATF4-mediated upregulation of one-carbon and folate pathways, as well as serine and proline catabolism (Bao et al., 2016; Forsström et al., 2019; Köhl et al., 2017; Szczepanowska et al., 2020). Therefore, we asked whether the mitoISR was induced in *Dars2*-deficient BMDMs and whether it was modulated by IL-4 + IL-13 stimulation. Notably, RNA-seq analysis revealed that *Dars2* deficiency increased expression of *Atf4* and *Ddit3/Chop*, encoding key transcription factors driving ISR, as well as several of their target genes, including *Trib3*, *Chac1*, *Slc1a4*, *Mthfd2*, *Shmt2*, *Slc7a5*,

(B) Western blot analysis of indicated targets in sorted peritoneal MΦs after treatment with IL-4c or NaCl. One technical replicate of n = 2 biological replicates per group.

(C) qRT-PCR analysis in sorted peritoneal MΦs after treatment with IL-4c or NaCl. One technical replicate of n = 2 biological replicates per genotype in the NaCl group, 6 per genotype in the IL-4c groups.

(D) Representative flow cytometry plots (n = 5 in total) of mitochondrial mass analysis by MTG fluorescent staining in sorted wound MΦs isolated from *Il4ra*<sup>fl/-</sup> and *Il4ra*<sup>MKO</sup> mice at 14 dpi. 7-AAD<sup>-</sup>CD11b<sup>+</sup>F4/80<sup>+</sup> cells were gated (G2) and the MFI of MTG was analyzed. One technical replicate of 5 biological replicates per genotype.

(E and F) EFA of OCR (E) and ECAR (F) in sorted wound MΦs isolated from *Il4ra*<sup>fl/-</sup> and *Il4ra*<sup>MKO</sup> mice at 14 dpi. (E) Cells were sequentially treated with oligomycin (Oligo), FCCP, and rotenone/antimycin A (R/A) as indicated. Six technical replicates for *Il4ra*<sup>fl/-</sup>, 8 for *Il4ra*<sup>MKO</sup> of 1 biological replicate per genotype. Left panel, the mean value ± SEM is represented.

\*p < 0.05, \*\*p < 0.01, \*\*\*p < 0.001 by one-way ANOVA with Tukey's multiple comparison test (A and C) or Student's unpaired two-tailed t test (D and E).



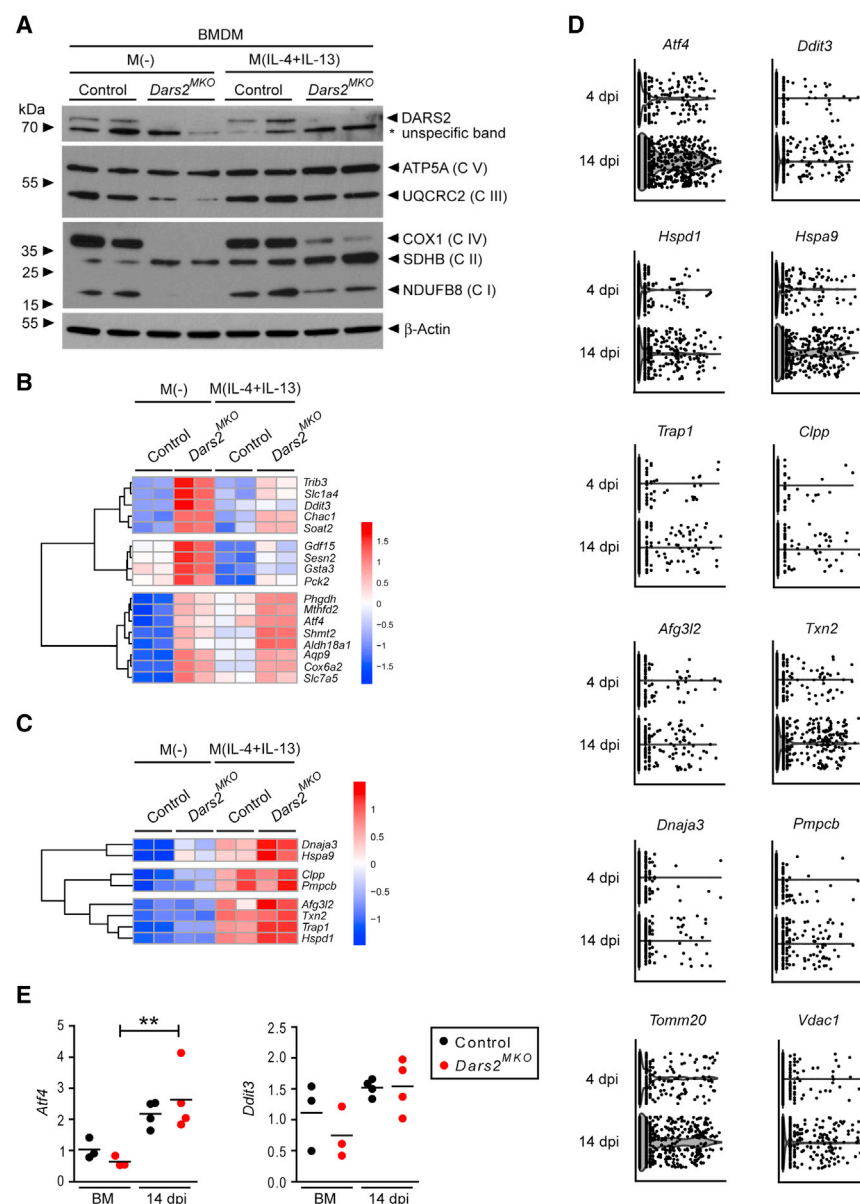


**Figure 7. Type-2 immune signals modulate mitochondrial stress responses and promote mitohormesis in wound MΦs**

(A) Western blot analysis of DARS2 and MRC complex subunits in BMDMs stimulated with IL-4 (50 ng/mL) and IL-13 (50 ng/mL) or vehicle for 48 h. 1 technical replicate of n = 2 biological replicates per group.

(B and C) HC showing the z-transformed expression values of ATF4 target genes associated with mitolSR (B) and genes associated with UPR<sup>mt</sup> (C) in BMDMs stimulated as described in (A). One technical replicate of n = 2 biological replicates per group.

(D) Violin plots showing individual genes after scRNA-seq in wound MΦs isolated at 4 and 14 dpi. (E) qRT-PCR analysis of gene expression in sorted wound MΦs normalized to blood monocytes. 1 technical replicate of n = 3 biological replicates per group for BM, 4 per group at 14 dpi. \*\*p < 0.01 by one-way ANOVA with Tukey's multiple comparison test. BM, blood monocytes.

DARS2, that already in untreated conditions displayed high upregulation of the same pathway (Figure 7B). Collectively, our findings demonstrate that type 2 immune signals can mitigate the negative impact that the absence of *Dars2* has on mitochondrial function.

During the latter part of the mitolSR the mitochondrial unfolded protein response (UPR<sup>mt</sup>) can be activated (Forssström et al., 2019). Indeed, unstimulated BMDMs did not display a transcriptional UPR<sup>mt</sup> signature regardless of the presence of *Dars2* (Figure 7C). Notably, IL-4 + IL-13 strongly induced UPR<sup>mt</sup> target genes (e.g., *Clpp*, *Afg3l2*, *Hspa9*, and *Hspd1*) independently of *Dars2* deficiency (Figure 7C), suggesting that type-2 immune signals strongly activate programs to increase mitochondrial fitness, including both UPR<sup>mt</sup> and mitolSR-regulated pathways (Figures 7B and 7C).

Cameron et al. previously detected similar changes in mitochondrial stress signatures in data obtained in similarly treated inflammatory BMDMs (Cameron et al., 2019). To determine whether this pathway is also conserved *in vivo*, we evaluated the prevalence of mitochondrial stress responses in wound MΦs, in the type-2-cytokine-dominated late-phase of skin wound healing by exploring our scRNA-seq dataset. Notably, we observed an enrichment of the important ISR transcription factors *Atf4* and *Ddit3* (CHOP) and of UPR<sup>mt</sup> target genes (*Hspd1*, *Hspa9*, *Trap1*, *Clpp*, *Afg3l2*, *Txn2*, *Dnaja3*, and *Pmpcb*) (Figure 7D) at 14 dpi compared with 4 dpi in line with our *in vitro* findings. Moreover, we found hallmark genes of mitochondrial biogenesis (*Tomm20* and *Vdac1*) enriched at 14 versus 4 dpi (Figure 7D), corroborating our mitochondrial mass analysis (Figure 1C). These findings link type-2 stimulation with the development of an UPR<sup>mt</sup>

and *Soat2* compared with unstimulated controls (Figure 7B). IL-4 + IL-13 stimulation partly attenuated the effects of *Dars2* deficiency on the expression of *Trib3*, *Slc1a4*, *Chac1*, and *Soat2* and abrogated the expression of *Ddit3/Chop* shown to be upregulated in conditions of persistent ISR leading to activation of pro-apoptotic genes and increased cell death (Figure 7B) (Costa-Mattoli and Walter, 2020; Marciniak et al., 2004). Notably, IL-4 + IL-13 stimulation of control BMDMs strongly decreased the expression of some of the mitolSR genes, including *Sesn2*, *Pck2*, *Gsta3*, and *Gdf15*, while normalizing their levels in *Dars2*-deficient cells compared with unstimulated cells (Figure 7B). In contrast, in control macrophages, IL-4 + IL-13 stimulation induced higher expression of mitolSR genes (*Atf4*, *Phgdh*, *Mthfd2*, *Slc7a5*, *Shmt2*, and *Aldh18a1*) involved in metabolic rewiring of one-carbon metabolism compared with unstimulated cells, while having milder effect in BMDMs lacking

and mitoISR transcriptional signature in MΦs during the skin repair response.

Given the effect that *Dars2* deficiency had on the expression of *Ddit3* (CHOP) and the ability of IL-4 + IL-13 to attenuate this defect, we hypothesized that in the late-phase of wound healing type 2 cytokines attenuate the mitoISR response, which would otherwise be induced by *Dars2* deficiency leading to increased cell death. Consistently, qRT-PCR in sorted wound MΦs revealed that the ISR transcription factors *Atf4* and *Ddit3* (CHOP) are expressed in *Dars2*-deficient and control cells at comparable levels at 14 dpi (Figure 7E). In summary, our data highlight a so far unknown functional link between IL-4 + IL-13 stimulation and regulation of mitochondrial stress responses that ultimately supports mitohormesis and ameliorates mitochondrial function.

## DISCUSSION

An important question in macrophage biology is what signals are required for the transition from pro-inflammatory clearance of infection or tissue injury to pro-resolution signals that rebuild tissue architecture and restore homeostasis. Here, we identify an *in vivo* causal link between the tissue repair response, cellular metabolism, and MΦ activation and function. Specifically, we show that during the subsequent phases of the tissue repair response, wound MΦs adopt distinct metabolic programs required to support different, phase-specific repair functions. While during the early-phase of repair, MΦs re-adjust their cellular metabolism by activating a glycolytic program, at the late-phase of repair, MΦs switch preferentially to OXPHOS. We propose that the dynamics of this phase-specific metabolic adaptation in injury-toward-repair-associated MΦs follows conceptually the framework of a recently proposed evolutionary perspective on immunometabolism (Wang et al., 2019). Thereby, glycolysis and anabolic metabolism represent key features of a maintenance program in immune cells with the aim of defense and protection (Wang et al., 2019). Consistently, we show that in early-phase wound MΦs, glycolysis enables injury-associated MΦs to rapidly produce a sufficient amount of ATP to carry out key effector and tissue protective functions, including pathogen defense and cytokine synthesis supporting tissue growth and promoting tissue integrity. In addition, we show that the glycolytic metabolic pathway in early-phase wound MΦs leads to increased production of lactate, a metabolite so far thought to be a major driver of pivotal early repair mechanisms, such as vascular sprouting (Hunt et al., 2007; Porporato et al., 2012; Trabold et al., 2003).

Another important function of glycolysis is to support anabolic processes by generating intermediates for biosynthesis, a key feature of regenerating tissues. Glycolysis is tightly linked with the PPP, which we show to be enriched in early-phase wound MΦs. Nucleotides produced in the PPP may be used for RNA synthesis and DNA replication to support proliferation of early-phase wound MΦs (Knipper et al., 2015). In addition, the PPP leads to the production of nicotinamide adenine dinucleotide phosphate (NADPH), which is required for fatty acid synthesis, ROS production by NADPH oxidase and glutathione synthesis as an antioxidant. Whereas ROS enable MΦs to clear invading pathogens from the early wound environment, antioxidants help to prevent tissue damage. Further, pyruvate generated by glycolysis in early-phase wound MΦs is likely to be directed to

the TCA cycle in the mitochondria, where it can be used for the synthesis of citrate and succinate (O'Neill and Pearce, 2016). In support of this assumption, we find that effective activation of early-phase wound MΦs requires both glycolysis and mitochondrial metabolism.

Indeed, an unexpected and important finding of our study is that myeloid cell-specific DARS2-deficiency causes impaired early wound inflammation and wound tissue vascularization, which ultimately hampers timely wound closure. Angiogenesis is at the core of an efficient repair response. We and others have shown that MΦs are the prevailing VEGF source for early wound vascularization (Gurevich et al., 2018; Willenborg et al., 2012). Yet, mechanisms regulating this early, MΦ-specific vascular response at the site of tissue injury are not yet entirely resolved. Here, we identify mtROS production in MΦs as an important regulator of HIF1 $\alpha$ -induced VEGF-A expression and MΦ-mediated wound angiogenesis. Our findings *in vivo* are consistent with earlier *in vitro* studies revealing mtROS as a critical regulator of HIF1 $\alpha$  stabilization (Chandel et al., 2000; Sumbayev, 2008; Tannahill et al., 2013).

Mills and colleagues have previously shown that the LPS-mediated increase of MMP and succinate oxidation in MΦs provide the driving force for reverse electron transport (RET) at C I and mtROS production, resulting in HIF1 $\alpha$  stabilization and expression of *I11b* (Mills et al., 2016). In our study, it remains an open question as to which MRC complex generates the mtROS critical for HIF1 $\alpha$  stabilization and *Vegfa* expression in early-phase wound MΦs. However, we see several lines of evidence that RET-mediated mtROS production at C I is occurring in pro-angiogenic wound macrophages. First, *Dars2*-deficient BMDMs are able to increase their MMP in response to LPS (a prerequisite for the occurrence of RET) and second, C I activity is absent in mitochondria isolated from *Dars2*-deficient BMDMs. Third, succinate metabolism is transcriptionally enriched in early-phase wound MΦs. Finally, we show that *I11b* expression is lower, and *I110* expression is higher in wound MΦs with reduced C I levels compared with controls, thereby supporting important features of succinate oxidation and RET.

In sharp contrast to the metabolism in early-phase MΦs, during the late-phase of healing, we find decreased expression of glycolytic enzymes and activation of catabolic processes such as ATP production by OXPHOS in wound MΦs. Notably, we show that OXPHOS in late-phase MΦs depends on IL-4R $\alpha$  activation. These findings are consistent with earlier reports demonstrating that after *in vitro* stimulation with IL-4 + IL-13 or *in vivo* infection with *H. polygyrus* in type-2-activated MΦs, FAO is induced and that the TCA cycle is intact and coupled to OXPHOS (Vats et al., 2006; Huang et al., 2014; Jha et al., 2015). With respect to the evolutionary perspective on immunometabolism (Wang et al., 2019), increased catabolism in late-phase wound MΦs may resemble the status of immune tolerance or dormancy to promote tissue protection and homeostasis during the repair response. Consistent with this view, we and others showed that type-2 immunity is an important regulator of repair and tolerance mechanisms in multiple tissues, including the skin (Knipper et al., 2015; Harris and Loke, 2017). Functionally, induction of FAO and intact TCA cycle/OXPHOS may allow late-phase wound MΦs to reduce inflammatory cytokine production, upregulate IL-10, and produce UDP-GlcNAc; all thought to be

important for the glycosylation of type-2-cytokine-induced scavenger receptors such as mannose receptor, which is a hallmark of IL-4R $\alpha$ -activated late-phase wound macrophages (Jha et al., 2015; Knipper et al., 2015; Malandrino et al., 2015). Further, FAO has been identified as a hallmark of immune cells with increased life span, such as IL-4-activated BMDMs and memory T cells (Vats et al., 2006; Michalek et al., 2011). Collectively, these findings imply that in late-phase wound M $\Phi$ s, enhanced OXPHOS levels support an effective adaptation to provide the metabolic requirements in M $\Phi$ s to carry out late-phase tissue-remodeling functions.

We present strong evidence for a so far unknown mechanism by which type-2 cytokines modulate mitochondrial stress responses in M $\Phi$ s. We show that exposure to IL-4 + IL-13 in wild-type BMDMs leads to induction of the UPR<sup>mt</sup> signature and the mitoISR signature associated with remodeling of one-carbon metabolism. Importantly, we detect a similar response also in late-stage wound M $\Phi$ s *in vivo*, under control of type-2 cytokines. Altered nuclear gene expression in response to moderate mitochondrial stress that subsequently makes the cell more resistant to subsequent stressors has been termed mitohormesis (Yun and Finkel, 2014). Interestingly, LPS- or hydroxyoestrogen-driven mitochondrial stress in BMDMs has been shown to trigger mitohormesis, which enforces LPS tolerance (Timblin et al., 2021). We propose that type-2 cytokines also induce a moderate mitochondrial stress thus triggering mitohormesis in M $\Phi$ s. During skin repair, this may increase the mitochondrial and cellular fitness of late-stage wound M $\Phi$ s, eventually e.g., prolonging their lifespan in the tissue and enabling them to exert their long-term tissue-remodeling functions.

In *Dars2*-deficient BMDMs already in the steady state, a mitoISR signature is detected, while the UPR<sup>mt</sup> activation is absent. This is consistent with the literature showing that in mammalian cells mitochondrial dysfunction activates an ATF4-mediated mitoISR rather than an ATF5-mediated UPR<sup>mt</sup> response (Bao et al., 2016; Quiros et al., 2017; Kaspar et al., 2021). Interestingly, a recent study revealed that inhibition of mitochondrial translation in T cells by the antibiotic linezolid induces folate-mediated one-carbon metabolism (a hallmark of mitoISR) with critical impact on Th17 effector function (Almeida et al., 2021). Notably, exposure of *Dars2*-deficient BMDMs to IL-4 + IL-13 partially normalizes the mitochondrial stress signatures to expression levels similar to controls, while maintaining upregulated one-carbon metabolism and increasing the UPR<sup>mt</sup> response. Therefore, type-2 cytokines seem to be able to ameliorate mitochondrial dysfunction, possibly by inducing mitohormetic responses. Together, here, we identify the induction of a mitochondrial stress signature as important hallmark of type-2 M $\Phi$ s activation. In future studies, it will be important to understand how type-2-mediated mitochondrial stress, OXPHOS, and type-2-mediated M $\Phi$  effector functions are connected. From the translational perspective, the question arises whether perturbed mitochondrial stress in myeloid cells contributes to pathological wound healing scenarios and whether modulating mitochondrial stress responses provide a target for therapeutic benefit.

### Limitations of the study

In our study, the exact source of mtROS, which is critical for HIF1 $\alpha$  stabilization and subsequently tissue vascularization, re-

mains open and merits further investigation. The identification of the relevant MRC complex could be critical e.g., for the development of therapeutic approaches.

Another limitation of our study is that we did not perform experiments in order to ameliorate the impaired wound healing response in *Dars2*<sup>MTKO</sup> mice. Therefore, future studies need to investigate whether our findings can be translated into an effective therapy.

### STAR★METHODS

Detailed methods are provided in the online version of this paper and include the following:

- KEY RESOURCES TABLE
- RESOURCE AVAILABILITY
  - Lead contact
  - Materials availability
  - Data and code availability
- EXPERIMENTAL MODEL AND SUBJECT DETAILS
  - Mouse Models
  - Cell culture
- METHOD DETAILS
  - Excisional punch injury
  - Adoptive transfer of RFP<sup>+</sup> monocytes
  - IL-4 complex-induced sterile peritonitis
  - Morphometric analysis
  - Immunostaining
  - Flow cytometry
  - Western blot analysis
  - Analysis of mitochondrial mass
  - Analysis of mitochondrial reactive oxygen species
  - Analysis of mitochondrial membrane potential by TMRM
  - Enzyme histochemistry to follow COX and SDH activities
  - Analysis of extracellular flux
  - Isolation of mitochondria
  - Blue native polyacrylamide gel electrophoresis (BN-PAGE) and *in-gel* activity
  - Quantitative Real-time PCR analysis
  - Bulk RNA sequencing of wound macrophages
  - Single-cell RNA sequencing of wound macrophages
  - RNA sequencing in BMDMs
- QUANTIFICATION AND STATISTICAL ANALYSIS
  - Data representation and statistical analysis

### SUPPLEMENTAL INFORMATION

Supplemental information can be found online at <https://doi.org/10.1016/j.cmet.2021.10.004>.

### ACKNOWLEDGMENTS

We thank Michael Piekarek, Gabriele Scherr, and Sebastian Wüst for excellent technical assistance; Dr. Gunter Rappl (Central Cell Sorting Facility, CMMC, Cologne University) for specialized technical support; Dr. Maria Patron (Max Planck Institute for Biology of Ageing, Cologne), and Prof. Ulrich Brandt (Radboud University Medical Center, Nijmegen, NL) for helpful discussions. This work was supported by the Deutsche Forschungsgemeinschaft (DFG, German Research Foundation): CRC829 (project number 73111208 to S.A.E. and

J.C.B.), the CRC1218 (project number 269925409 to S.A.E., A.T., and T.L.), the Research Unit FOR2599 (project number 3927 49992 to S.A.E., E.J.P., and A.R.); the CRC1403 (project number 414786233 to S.A.E.), Germany's Excellence Strategy – CECAD, EXC 2030 – 390661388 to S.A.E., J.C.B., T.L., and A.T.; Research Unit FOR2240 (EM48/5-2 to S.A.E.), Center for Molecular Medicine (to S.A.E., J.C.B., and A.T.), and the DEBRA International Foundation (to S.A.E.).

## AUTHOR CONTRIBUTIONS

S.W. and S.A.E. wrote the manuscript; S.W. designed and performed most of the experiments and analyzed the data; S.A.E. conceived and supervised the study; A.J. and J.C.B. performed and analyzed the extracellular flux analysis; T.U. and J.L.S. performed and analyzed the bulk RNA-seq analysis; D.E.S. and E.J.P. conceptualized experiments and performed the scRNA-seq analysis and the RNA-seq analysis of BMDMs; M.P. and A.T. performed the analysis in mitochondria isolates; X.D. and J.N. performed the Western blot analysis; A.G. and A.R. performed the adoptive transfer experiments; T.M.V. and T.L. supported the analysis of mtROS and mitochondrial mass; A.T. generated the *Dars2* flox mice; all authors commented on and edited the manuscript.

## DECLARATION OF INTERESTS

The authors declare no competing interests.

## INCLUSION AND DIVERSITY

We worked to ensure sex balance in the selection of non-human subjects.

Received: July 12, 2021

Revised: September 7, 2021

Accepted: October 5, 2021

Published: October 28, 2021

## REFERENCES

- Almeida, L., Dhillon-Labrooy, A., Castro, C.N., Adossa, N., Carriche, G.M., Guderian, M., Lippens, S., Dennerlein, S., Hesse, C., Lambrecht, B.N., et al. (2021). Ribosome-targeting antibiotics impair T cell effector function and ameliorate autoimmunity by blocking mitochondrial protein synthesis. *Immunity* 54, 68–83.e6.
- Askenase, M.H., Goods, B.A., Beatty, H.E., Steinschneider, A.F., Velazquez, S.E., Oshero, A., Landreneau, M.J., Carroll, S.L., Tran, T.B., Avram, V.S., et al. (2021). Longitudinal transcriptomics define the stages of myeloid activation in the living human brain after intracerebral hemorrhage. *Sci. Immunol.* 6, eabd6279.
- Bao, X.R., Ong, S.E., Goldberger, O., Peng, J., Sharma, R., Thompson, D.A., Vafai, S.B., Cox, A.G., Marutani, E., Ichinose, F., et al. (2016). Mitochondrial dysfunction remodels one-carbon metabolism in human cells. *Elife* 5, e10575.
- Bhardwaj, V., Semplicio, G., Erdogdu, N.U., Manke, T., and Akhtar, A. (2019). MAPCap allows high-resolution detection and differential expression analysis of transcription start sites. *Nat. Commun.* 10, 3219.
- Bosurgi, L., Cao, Y.G., Cabeza-Cabrero, M., Tucci, A., Hughes, L.D., Kong, Y., Weinstein, J.S., Licona-Limon, P., Schmid, E.T., Pelorosso, F., et al. (2017). Macrophage function in tissue repair and remodeling requires IL-4 or IL-13 with apoptotic cells. *Science* 356, 1072–1076.
- Cameron, A.M., Castoldi, A., Sanin, D.E., Flachsmann, L.J., Field, C.S., Puleston, D.J., Kyle, R.L., Patterson, A.E., Hässler, F., Buescher, J.M., et al. (2019). Inflammatory macrophage dependence on NAD<sup>+</sup> salvage is a consequence of reactive oxygen species-mediated DNA damage. *Nat. Immunol.* 20, 420–432.
- Chandel, N.S., McClintock, D.S., Feliciano, C.E., Wood, T.M., Melendez, J.A., Rodriguez, A.M., and Schumacker, P.T. (2000). Reactive oxygen species generated at mitochondrial complex III stabilize hypoxia-inducible factor-1α during hypoxia: a mechanism of O<sub>2</sub> sensing. *J. Biol. Chem.* 275, 25130–25138.

- Clausen, B.E., Burkhardt, C., Reith, W., Renkawitz, R., and Förster, I. (1999). Conditional gene targeting in macrophages and granulocytes using LysMcre mice. *Transgenic. Res.* 8, 265–277.
- Corliss, B.A., Azimi, M.S., Munson, J.M., Peirce, S.M., and Murfee, W.L. (2016). Macrophages: an inflammatory link Between angiogenesis and lymphangiogenesis. *Microcirculation* 23, 95–121.
- Costa-Mattioli, M., and Walter, P. (2020). The integrated stress response: From mechanism to disease. *Science* 368, eaat5314.
- Dobin, A., Davis, C.A., Schlesinger, F., Drenkow, J., Zaleski, C., Jha, S., Batut, P., Chaisson, M., and Gingeras, T.R. (2013). STAR: ultrafast universal RNA-seq aligner. *Bioinformatics* 29, 15–21.
- Dogan, S.A., Pujol, C., Maiti, P., Kukut, A., Wang, S., Hermans, S., Senft, K., Wibom, R., Rugari, E.I., and Trifunovic, A. (2014). Tissue-specific loss of DARS2 activates stress responses independently of respiratory chain deficiency in the heart. *Cell Metab.* 19, 458–469.
- Eming, S.A., Murray, P.J., and Pearce, E.J. (2021). Metabolic orchestration of the wound healing response. *Cell Metab.* 33, 1726–1743.
- Eming, S.A., Wynn, T.A., and Martin, P. (2017). Inflammation and metabolism in tissue repair and regeneration. *Science* 356, 1026–1030.
- Forsström, S., Jackson, C.B., Carroll, C.J., Kuronen, M., Pirinen, E., Pradhan, S., Marmyleva, A., Auranen, M., Kleine, I.-M., Khan, N.A., et al. (2019). Fibroblast growth factor 21 drives dynamics of local and systemic stress responses in mitochondrial myopathy with mtDNA deletions. *Cell Metab.* 30, 1040–1054.e7.
- Gause, W.C., Wynn, T.A., and Allen, J.E. (2013). Type 2 immunity and wound healing: evolutionary refinement of adaptive immunity by helminths. *Nat. Rev. Immunol.* 13, 607–614.
- Gurevich, D.B., Severn, C.E., Twomey, C., Greenhough, A., Cash, J., Toye, A.M., Mellor, H., and Martin, P. (2018). Live imaging of wound angiogenesis reveals macrophage orchestrated vessel sprouting and regression. *EMBO J.* 37, e97786.
- Gurtner, G.C., Werner, S., Barrandon, Y., and Longaker, M.T. (2008). Wound repair and regeneration. *Nature* 453, 314–321.
- Hafemeister, C., and Satija, R. (2019). Normalization and variance stabilization of single-cell RNA-seq data using regularized negative binomial regression. *Genome Biol.* 20, 296.
- Hao, Y., Hao, S., Andersen-Nissen, E., Mauck, W.M., 3<sup>rd</sup>, Zheng, S., Butler, A., Lee, M.J., Wilk, A.J., Darby, C., Zager, M., et al. (2021). Integrated analysis of multimodal single-cell data. *Cell* 184, 3573–3587.e29.
- Harris, N.L., and Loke, P. (2017). Recent advances in type-2-cell-mediated immunity: insights from helminth infection. *Infect. Immun.* 47, 1024–1036.
- Herbert, D.R., Hölscher, C., Mohrs, M., Arendse, B., Schwegmann, A., Radwanska, M., Leeto, M., Kirsch, R., Hall, P., Mossman, H., et al. (2004). Alternative macrophage activation is essential for survival during schistosomiasis and downmodulates T helper 1 responses and immunopathology. *Immunity* 20, 623–635.
- Huang, S.C.-C., Everts, B., Ivanova, Y., O'Sullivan, D., Nascimento, M., Smith, A.M., Beatty, W., Love-Gregory, L., Lam, W.Y., O'Neill, C.M., et al. (2014). Cell-intrinsic lysosomal lipolysis is essential for alternative activation of macrophages. *Nat. Immunol.* 15, 846–855.
- Huang, S.C.-C., Smith, A.M., Everts, B., Colonna, M., Pearce, E.L., Schilling, J.D., and Pearce, E.J. (2016). Metabolic reprogramming mediated by the mTORC2-IRF4 signaling axis is essential for macrophage alternative activation. *Immunity* 45, 817–830.
- Hunt, T.K., Aslam, R.S., Beckert, S., Wagner, S., Ghani, Q.P., Hussain, M.Z., Roy, S., and Sen, C.K. (2007). Aerobically derived lactate stimulates revascularization and tissue repair via redox mechanisms. *Antioxid. Redox Signal.* 9, 1115–1124.
- Jenkins, S.J., Ruckerl, D., Cook, P.C., Jones, L.H., Finkelman, F.D., van Rooijen, N., MacDonald, A.S., and Allen, J.E. (2011). Local macrophage proliferation, rather than recruitment from the blood, is a signature of TH2 inflammation. *Science* 332, 1284–1288.
- Jha, A.K., Huang, S.C.-C., Sergushichev, A., Lampropoulou, V., Ivanova, Y., Loginicheva, E., Chmielewski, K., Stewart, K.M., Ashall, J., Everts, B., et al.



- (2015). Network integration of parallel metabolic and transcriptional data reveals metabolic modules that regulate macrophage polarization. *Immunity* 42, 419–430.
- Kaspar, S., Oertlin, C., Szczepanowska, K., Kukat, A., Senft, K., Lucas, C., Brodesser, S., Hatzoglou, M., Larsson, O., Topisirovic, I., and Trifunovic, A. (2021). Adaptation to mitochondrial stress requires CHOP-directed tuning of ISR. *Sci. Adv.* 7, eabf0971.
- Knipper, J.A., Willenborg, S., Brinckmann, J., Bloch, W., Maaß, T., Wagener, R., Krieg, T., Sutherland, T., Munitz, A., Rothenberg, M.E., et al. (2015). Interleukin-4 receptor  $\alpha$  signaling in myeloid cells controls collagen fibril assembly in skin repair. *Immunity* 43, 803–816.
- Kühl, I., Miranda, M., Atanassov, I., Kuznetsova, I., Hinze, Y., Mourier, A., Filipovska, A., and Larsson, N.-G. (2017). Transcriptomic and proteomic landscape of mitochondrial dysfunction reveals secondary coenzyme Q deficiency in mammals. *Elife* 6, e30952.
- Lallemand, Y., Luria, V., Haffner-Krausz, R., and Lonai, P. (1998). Maternally expressed PGK-CreTransgene as a tool for early and uniform activation of the Cre site-specific recombinase. *Transgenic. Res.* 7, 105–112.
- Langmead, B., and Salzberg, S.L. (2012). Fast gapped-read alignment with Bowtie 2. *Nat. Methods* 9, 357–359.
- Liao, Y., Smyth, G.K., and Shi, W. (2014). featureCounts: an efficient general purpose program for assigning sequence reads to genomic features. *Bioinformatics* 30, 923–930.
- Love, M.I., Huber, W., and Anders, S. (2014). Moderated estimation of fold change and dispersion for RNA-seq data with DESeq2. *Genome Biol.* 15, 550.
- Lucas, T., Waisman, A., Ranjan, R., Roes, J., Krieg, T., Müller, W., Roers, A., and Eming, S.A. (2010). Differential roles of macrophages in diverse phases of skin repair. *J. Immunol.* 184, 3964–3977.
- Luche, H., Weber, O., Nageswara Rao, T., Blum, C., and Fehling, H.J. (2007). Faithful activation of an extra-bright red fluorescent protein in “knock-in” Cre-reporter mice ideally suited for lineage tracing studies. *Eur. J. Immunol.* 37, 43–53.
- Malandrino, M.I., Fucho, R., Weber, M., Calderon-Dominguez, M., Mir, J.F., Valcarcel, L., Escoté, X., Gómez-Serrano, M., Peral, B., Salvadó, L., et al. (2015). Enhanced fatty acid oxidation in adipocytes and macrophages reduces lipid-induced triglyceride accumulation and inflammation. *Am. J. Physiol. Endocrinol. Metab.* 308, E756–E769.
- Marciniak, S.J., Yun, C.Y., Oyadomari, S., Novoa, I., Zhang, Y., Jungreis, R., Nagata, K., Harding, H.P., and Ron, D. (2004). CHOP induces death by promoting protein synthesis and oxidation in the stressed endoplasmic reticulum. *Genes Dev.* 18, 3066–3077.
- Martin, M. (2011). Cutadapt removes adapter sequences from high-throughput sequencing reads. *EMBnet J.* 17, 10–12. <https://doi.org/10.14806/ej.17.1.200>.
- McInnes, L., Healy, J., Saul, N., and Großberge, L. (2018). UMAP: uniform manifold approximation and projection. *J. Open Source Softw.* 3, 861. <https://doi.org/10.21105/joss.00861>.
- Michalek, R.D., Gerriets, V.A., Jacobs, S.R., Macintyre, A.N., MacIver, N.J., Mason, E.F., Sullivan, S.A., Nichols, A.G., and Rathmell, J.C. (2011). Cutting edge: distinct glycolytic and lipid oxidative metabolic programs are essential for effector and regulatory CD4<sup>+</sup> T cell subsets. *J. Immunol.* 186, 3299–3303.
- Millis, E.L., Kelly, B., Logan, A., Costa, A.S.H., Varma, M., Bryant, C.E., Tourlomousis, P., Däbritz, J.H.M., Gottlieb, E., Latorre, I., et al. (2016). Succinate dehydrogenase supports metabolic repurposing of mitochondria to drive inflammatory macrophages. *Cell* 167, 457–470.e13.
- Mirza, R., DiPietro, L.A., and Koh, T.J. (2009). Selective and specific macrophage ablation is detrimental to wound healing in mice. *Am. J. Pathol.* 175, 2454–2462.
- Murphy, M.P. (2009). How mitochondria produce reactive oxygen species. *Biochem. J.* 417, 1–13.
- Murray, P.J., and Wynn, T.A. (2011). Protective and pathogenic functions of macrophage subsets. *Nat. Rev. Immunol.* 11, 723–737.
- O'Neill, L.A., and Pearce, E.J. (2016). Immunometabolism governs dendritic cell and macrophage function. *J. Exp. Med.* 213, 15–23.
- Pedersen, T.L. (2020). patchwork: the composer of plots. R package version 1.1.1. <https://CRAN.R-project.org/package=patchwork>.
- Picelli, S., Faridani, O.R., Björklund, A.K., Winberg, G., Sagasser, S., and Sandberg, R. (2014). Full-length RNA-Seq from single cells using Smart-seq2. *Nat. Protoc.* 9, 171–181.
- Porporato, P.E., Payen, V.L., De Saedelee, C.J., Pr  at, V., Thissen, J.-P., Feron, O., and Sonveaux, P. (2012). Lactate stimulates angiogenesis and accelerates the healing of superficial and ischemic wounds in mice. *Angiogenesis* 15, 581–592.
- Quir  s, P.M., Prado, M.A., Zamboni, N., D'Amico, D., Williams, R.W., Finley, D., Gygi, S.P., and Auwerx, J. (2017). Multi-omics analysis identifies ATF4 as a key regulator of the mitochondrial stress response in mammals. *J. Cell Biol.* 216, 2027–2045.
- Rambold, A.S., and Pearce, E.L. (2018). Mitochondrial dynamics at the interface of immune cell metabolism and function. *Trends Immunol.* 39, 6–18.
- Ram  rez, F., Ryan, D.P., Gr  ning, B., Bhardwaj, V., Kilpert, F., Richter, A.S., Heyne, S., D  ndar, F., and Manke, T. (2016). deepTools2: a next generation web server for deep-sequencing data analysis. *Nucleic Acids Res.* 44, W160–W165.
- R v. 4.0.0. <http://www.R-project.org/>.
- Rodr  guez-Prados, J.-C., Trav  s, P.G., Cuenca, J., Rico, D., Aragon  s, J., Martin-Sanz, P., Cascante, M., and Bosc  , L. (2010). Substrate fate in activated macrophages: a comparison between innate, classic, and alternative activation. *J. Immunol.* 185, 605–614.
- Sanin, D.E., Matsushita, M., Klein Geltink, R.I., Grzes, K.M., van Teijlingen Bakker, N., Corrado, M., Kabat, A.M., Buck, M.D., Qiu, J., Lawless, S.J., et al. (2018). Mitochondrial membrane potential regulates nuclear gene expression in macrophages exposed to prostaglandin E2. *Immunity* 49, 1021–1033.e6.
- Schneider, C.A., Rasband, W.S., and Eliceiri, K.W. (2012). NIH Image to ImageJ: 25 years of image analysis. *Nat. Methods* 9, 671–675.
- Stuart, T., Butler, A., Hoffman, P., Hafemeister, C., Papalexi, E., Mauck, W.M., 3rd, Hao, Y., Stoeckius, M., Smibert, P., and Satija, R. (2019). Comprehensive integration of single-cell data. *Cell* 177, 1888–1902.e21.
- Sumbayev, V.V. (2008). LPS-induced toll-like receptor 4 signalling triggers cross-talk of apoptosis signal-regulating kinase 1 (ASK1) and HIF-1 $\alpha$  protein. *FEBS Lett.* 582, 319–326.
- Szczepanowska, K., Senft, K., Heidler, J., Herholz, M., Kukat, A., H  hne, M.N., Hofsetz, E., Becker, C., Kaspar, S., Giese, H., et al. (2020). A salvage pathway maintains highly functional respiratory complex I. *Nat. Commun.* 11, 1643.
- Tannahill, G.M., Curtis, A.M., Adamik, J., Palsson-McDermott, E.M., McGettrick, A.F., Goel, G., Frezza, C., Bernard, N.J., Kelly, B., Foley, N.H., et al. (2013). Succinate is an inflammatory signal that induces IL-1 $\beta$  through HIF-1 $\alpha$ . *Nature* 496, 238–242.
- Tenenbaum, D. (2020). KEGGREST: client-side REST access to KEGG. R package version 1.28.0. <https://bioconductor.org/packages/release/bioc/html/KEGGREST.html>.
- Timblin, G.A., Tharp, K.M., Ford, B., Winchester, J.M., Wang, J., Zhu, S., Khan, R.I., Louie, S.K., Iavarone, A.T., Ten Hoeve, J.T., et al. (2021). Mitohormesis reprogrammes macrophage metabolism to enforce tolerance. *Nat. Metab.* 3, 618–635.
- Trabold, O., Wagner, S., Wicke, C., Scheuenstuhl, H., Hussain, M.Z., Rosen, N., Seremetiev, A., Becker, H.D., and Hunt, T.K. (2003). Lactate and oxygen constitute a fundamental regulatory mechanism in wound healing. *Wound Repair Regen.* 11, 504–509.
- Vats, D., Mukundan, L., Odegaard, J.I., Zhang, L., Smith, K.L., Morel, C.R., Wagner, R.A., Greaves, D.R., Murray, P.J., and Chawla, A. (2006). Oxidative metabolism and PGC-1 $\beta$  attenuate macrophage-mediated inflammation. *Cell Metab.* 4, 13–24.
- Wang, A., Luan, H.H., and Medzhitov, R. (2019). An evolutionary perspective on immunometabolism. *Science* 363, 6423.
- Wickham, H. (2016). ggplot2: Elegant Graphics for Data Analysis (Springer).
- Willenborg, S., Lucas, T., van Loo, G., Knipper, J.A., Krieg, T., Haase, I., Brachvogel, B., Hammerschmidt, M., Nagy, A., Ferrara, N., et al. (2012).

CCR2 recruits an inflammatory macrophage subpopulation critical for angiogenesis in tissue repair. *Blood* 120, 613–625.

Wu, T.D., and Nacu, S. (2010). Fast and SNP-tolerant detection of complex variants and splicing in short reads. *Bioinformatics* 26, 873–881.

Yun, J., and Finkel, T. (2014). Mitohormesis. *Cell Metab.* 19, 757–766.

Zappia, L., and Oshlack, A. (2018). Clustering trees: a visualization for evaluating clusterings at multiple resolutions. *GigaScience* 7, giy083. <https://doi.org/10.1093/gigascience/giy083>.

Zhang, D., Tang, Z., Huang, H., Zhou, G., Cui, C., Weng, Y., Liu, W., Kim, S., Lee, S., Perez-Neut, M., et al. (2019). Metabolic regulation of gene expression by histone lactylation. *Nature* 574, 575–580.

## STAR★METHODS

### KEY RESOURCES TABLE

REAGENT or RESOURCE	SOURCE	IDENTIFIER
<b>Antibodies</b>		
Alexa Fluor 488 goat anti-rat	Thermo Fisher Scientific	Cat# A-11066; RRID: AB_2534074
APC Rat anti-mouse CD11b (M1/70)	Thermo Fisher Scientific	Cat# 17-0112-82; RRID: AB_467108
APC-Cy7 Rat anti-mouse CD11b (M1/70)	Thermo Fisher Scientific	Cat# A15390; RRID: AB_2534404
Biotin Armenian Hamster anti-mouse CD3e (145-2C11)	Thermo Fisher Scientific	Cat# 13-0031-82; RRID: AB_466319
Biotin Mouse anti-mouse NK1.1 (PK136)	Thermo Fisher Scientific	Cat# 13-5941-82; RRID: AB_466804
Biotin Rat anti-mouse CD4 (GK1.5)	Thermo Fisher Scientific	Cat# 13-0041-82; RRID: AB_466325
Biotin Rat anti-mouse CD19 (eBio1D3)	Thermo Fisher Scientific	Cat# 13-0193-82; RRID: AB_657656
Biotin Rat anti-mouse CD45R (RA3-6B2)	BioLegend	Cat# 103203; RRID: AB_312989
Biotin Rat anti-mouse CD117 (2B8)	BioLegend	Cat# 105804; RRID: AB_313213
Biotin Rat anti-mouse CD49b (DX5)	BioLegend	Cat# 108904; RRID: AB_313411
Biotin Rat anti-mouse Ly-6G (1A8)	BioLegend	Cat# 127604; RRID: AB_1186108
Biotin Rat anti-mouse TER-119 (TER-119)	BioLegend	Cat# 116204; RRID: AB_313705
eFluor450 Rat anti-mouse CD45 (30-F11)	Thermo Fisher Scientific	Cat# 48-0451-82; RRID: AB_1518806
FITC Rat anti-mouse CD45 (30-F11)	Thermo Fisher Scientific	Cat# 11-0451-82; RRID: AB_465050
HRP Rabbit anti-mouse IG	Dako	Cat# P0260; RRID: AB_2636929
HRP Swine anti-rabbit IG	Dako	Cat# P0399; RRID: AB_2617141
MicroBeads anti-Biotin	Miltenyi Biotec	Cat# 130-090-485; RRID: AB_244365
Mouse anti-ATP5A (15H4C4)	Abcam	Cat# ab14748; RRID: AB_301447
Mouse anti- $\beta$ -actin (C4)	Sigma-Aldrich	Cat# MAB1501; RRID: AB_2223041
Mouse anti-MT-CO1 (1D6E1A8)	Thermo Fisher Scientific	Cat# 459600; RRID: AB_2532240
Mouse anti-NDUFA9 (20C11B11B11)	Thermo Fisher Scientific	Cat# 459100; RRID: AB_2532223
Mouse anti-OxPhos Complex IV subunit IV (20E8C12)	Thermo Fisher Scientific	Cat# A21348; RRID: AB_2535839
Mouse anti-SDHA (2E3GC12FB2AE2)	Thermo Fisher Scientific	Cat# 459200; RRID: AB_2532231
Mouse anti-UQCRC1 (16D10AD9AH5)	Thermo Fisher Scientific	Cat# 459140; RRID: AB_2532227
PE Rat anti-mouse F4/80 (Cl:A3-1)	Bio-Rad Laboratories	Cat# MCA497PE; RRID: 2098196
Rabbit anti-HIF-1 alpha	Novus Biologicals	Cat# NB100-449; RRID: 10001045
Rabbit anti-DARS2	Proteintech	Cat# 13807-1-AP; RRID: 2088759
Rat anti-mouse IL-4 (11B11)	Bio X Cell	Cat# BP0045; RRID: AB_1107707
Rat anti-Ly-6C (AL-21)	BD Biosciences	Cat# 560595; RRID: AB_1727554
Rat anti-mouse CD115 (AFS98)	Thermo Fisher Scientific	Cat# 17-1152-82; RRID: AB_1210789
Rat anti-mouse CD115 (AFS98)	BioLegend	Cat# 135502; RRID: AB_1937293
Rat anti-mouse CD31 (MEC 13.3)	BD Biosciences	Cat# 553370; RRID: AB_396660
Rat anti-mouse CD16/CD32	Thermo Fisher Scientific	Cat# 14-0161-82; RRID: AB_467133
Total OXPHOS Rodent WB Antibody Cocktail	Abcam	Cat# ab110413; RRID: AB_2629281
<b>Chemicals, peptides, and recombinant proteins</b>		
Acetone	Roth	Cat# 5025.6; CAS# 67-64-1
Antimycin A	Sigma-Aldrich	Cat# A8674; CAS# 1397-94-0
Bradford	Sigma-Aldrich	Cat# B6916
Catalase from bovine liver	Sigma-Aldrich	Cat# C9322
Cytochrome c from equine heart	Sigma-Aldrich	Cat# C2506
DAPI (4',6-diamidino-2-phenylindole)	Thermo Fisher Scientific	Cat# D21490
DDM (Dodecylmaltoside)	Sigma-Aldrich	Cat# D4641; CAS# 69227-93-6

(Continued on next page)

**Continued**

REAGENT or RESOURCE	SOURCE	IDENTIFIER
Diethyl succinate	Sigma-Aldrich	Cat# 112402; CAS# 123-25-1
FCCP (Carbonyl cyanide 4-(trifluoromethoxy) phenylhydrazone)	Sigma-Aldrich	Cat# C2920; CAS# 370-86-5
Liberase™ TM Research Grade	Roche	Cat# 5401119001
Lipopolysaccharides from Escherichia coli O55:B5	Sigma-Aldrich	Cat# L2880
M-CSF	Peptotech	Cat# 315-02
MitoSOX™ Red Mitochondrial Superoxide Indicator	Thermo Fisher Scientific	Cat# M36008
MitoTracker™ Green FM	Thermo Fisher Scientific	Cat# M7514
NADH	Sigma-Aldrich	Cat# 10107735001; CAS# 606-68-8
Nitroblue tetrazolium	Sigma-Aldrich	Cat# N6876; CAS# 298-83-9
O.C.T. compound	Fisher Scientific	Cat# 12351753
Oligomycin	Sigma-Aldrich	Cat# O4876; CAS# 1404-19-9
Phenazine methosulfate	Sigma-Aldrich	Cat# P9625; CAS# 299-11-6
PhosSTOP™	Roche	Cat# 04906837001
Power SYBR™ Green PCR Master Mix	Thermo Fisher Scientific	Cat# 4368708
Recombinant Murine IL-4	Peptotech	Cat# 214-14
Recombinant Murine IL-13	Peptotech	Cat# 210-13
Recombinant Murine IFN $\gamma$	Peptotech	Cat# 315-05
Rotenone	Sigma-Aldrich	Cat# R8875; CAS# 83-79-4
ROTI®Block	Roth	Cat# A151.2
Roti®HistoFix 4% formaldehyde	Roth	Cat# P087.1
Sodium azide	Sigma-Aldrich	Cat# S8032; CAS# 26628-22-8
Sodium succinate dibasic hexahydrate	Sigma-Aldrich	Cat# S2378; CAS# 6106-21-4
TMRM (Tetramethylrhodamine, Methyl Ester, Perchlorate)	Thermo Fisher Scientific	Cat# T668
TRIzol	Thermo Fisher Scientific	Cat# 10296010
Western Lightning ECL Pro	PerkinElmer	Cat# NEL120001EA
3,3'-Diaminobenzidine tetrahydrochloride hydrate	Sigma-Aldrich	Cat# D9015; CAS# 868272-85-9
7-AAD (7-Aminoactinomycin D)	Thermo Fisher Scientific	Cat# 00-6993-50

**Critical commercial assays**

CyQUANT™ Cell Proliferation Assay	Thermo Fisher Scientific	Cat# C7026
High-Capacity cDNA Reverse Transcription Kit	Thermo Fisher Scientific	Cat# 4368813
KAPA Taq Extra HotStart ReadyMix	Sigma-Aldrich	Cat# KK3605
Micro BCA™ Protein Assay Kit	Thermo Fisher Scientific	Cat# 23235
QuantStudio™ 5 Real-Time PCR System, 384-well	Thermo Fisher Scientific	Cat# A28575
RNeasy Plus Micro Kit	Qiagen	Cat# 74034
RNeasy Plus Mini Kit	Qiagen	Cat# 74134
Seahorse extracellular flux analyzer Xfe 96	Agilent	<a href="https://www.agilent.com/en/product/cell-analysis/real-time-cell-metabolic-analysis/xf-analyzers/seahorse-xfe96-analyzer-740879">https://www.agilent.com/en/product/cell-analysis/real-time-cell-metabolic-analysis/xf-analyzers/seahorse-xfe96-analyzer-740879</a>
TruePrep Index Kit V2 for Illumina	Vazyme	TD202
TruSeq RNA Library Prep Kit v2	Illumina	Cat# RS-122-2001

**Deposited data**

RNA-Seq wound macrophages	This paper	NCBI GEO: GSE157291; <a href="https://www.ncbi.nlm.nih.gov/geo/query/acc.cgi?acc=GSE157291">https://www.ncbi.nlm.nih.gov/geo/query/acc.cgi?acc=GSE157291</a>
Single-cell RNA-seq wound macrophages	This paper	NCBI GEO: GSE183489; <a href="https://www.ncbi.nlm.nih.gov/geo/query/acc.cgi?acc=GSE183489">https://www.ncbi.nlm.nih.gov/geo/query/acc.cgi?acc=GSE183489</a>
RNA-Seq BMDM	This paper	NCBI GEO: GSE183488; <a href="https://www.ncbi.nlm.nih.gov/geo/query/acc.cgi?acc=GSE183488">https://www.ncbi.nlm.nih.gov/geo/query/acc.cgi?acc=GSE183488</a>

(Continued on next page)



**Continued**

REAGENT or RESOURCE	SOURCE	IDENTIFIER
Experimental models: Organisms/strains		
<i>Dars2<sup>loxP/loxP</sup></i> mice	Dogan et al., 2014	N/A
<i>Lyz2-cre</i> mice	Clausen et al., 1999	N/A
<i>Dars2<sup>loxP/loxP</sup></i> <i>Lyz2-cre</i> mice, <i>Dars2<sup>MKO</sup></i>	This paper	N/A
<i>Il4ra<sup>fl/fl</sup></i> <i>Lyz2-cre</i> , <i>Il4ra<sup>MKO</sup></i>	Herbert et al., 2004	N/A
C57BL/6J mice	Charles River	<a href="https://www.criver.com/products-services/find-model/jax-c57bl6j-mice?region=23">https://www.criver.com/products-services/find-model/jax-c57bl6j-mice?region=23</a>
C57BL/6JRj mice	Janvier	<a href="https://www.janvier-labs.com/en/fiche_produit/c57bl-6jrj_mouse/">https://www.janvier-labs.com/en/fiche_produit/c57bl-6jrj_mouse/</a>
B6.RFP mice	Lallemant et al., 1998; Luche et al., 2007	N/A
Oligonucleotides		
See Table S1 for primer sequences used for genotyping and qRT-PCR analysis		
Software and algorithms		
Bowtie2 version 2.2.1	Langmead and Salzberg, 2012	<a href="http://bowtie-bio.sourceforge.net/bowtie2/index.shtml">http://bowtie-bio.sourceforge.net/bowtie2/index.shtml</a>
BZ-11 viewer software	Keyence	<a href="https://www.keyence.de/landing/microscope/lp_fluorescence.jsp">https://www.keyence.de/landing/microscope/lp_fluorescence.jsp</a>
Diskus 4.8 software	Hilgers Technical Office	<a href="https://diskus-viewer.software.informer.com/">https://diskus-viewer.software.informer.com/</a>
DESeq2 v. 1.28.1	Love et al., 2014	<a href="https://bioconductor.org/packages/release/bioc/html/DESeq2.html">https://bioconductor.org/packages/release/bioc/html/DESeq2.html</a>
Seurat v. 4.0.2	Hao et al., 2021	<a href="https://cran.r-project.org/web/packages/Seurat/index.html">https://cran.r-project.org/web/packages/Seurat/index.html</a>
Clustree v. 0.4.3	Zappia and Oshlack, 2018	<a href="https://cran.r-project.org/web/packages/clustree/index.html">https://cran.r-project.org/web/packages/clustree/index.html</a>
ggplot2 v. 3.3.5	Wickham, 2016	<a href="https://cran.r-project.org/web/packages/ggplot2/index.html">https://cran.r-project.org/web/packages/ggplot2/index.html</a>
Patchwork v. 1.1.1	Pedersen, 2020	<a href="https://CRAN.R-project.org/package=patchwork">https://CRAN.R-project.org/package=patchwork</a>
KEGGREST v. 1.28	Tenenbaum, 2020.	<a href="https://bioconductor.statistik.tu-dortmund.de/packages/3.11/bioc/html/KEGGREST.html">https://bioconductor.statistik.tu-dortmund.de/packages/3.11/bioc/html/KEGGREST.html</a>
G*Power 3.1.9.2	Heinrich-Heine-Universität Düsseldorf	<a href="https://gpower.software.informer.com/download/">https://gpower.software.informer.com/download/</a>
ImageJ 1.47t	Schneider et al., 2012	<a href="https://imagej.nih.gov/ij/index.html">https://imagej.nih.gov/ij/index.html</a>
FACSDiva Version 6.1.1	BD Biosciences	<a href="https://www.bdbiosciences.com/en-de/products/software/instrument-software/bd-facsddiva-software">https://www.bdbiosciences.com/en-de/products/software/instrument-software/bd-facsddiva-software</a>
FlowJo Version 10.7.1	FlowJo	<a href="https://www.flowjo.com/">https://www.flowjo.com/</a>
GraphPad Prism 8	GraphPad Prism	<a href="https://www.graphpad.com/scientific-software/prism/">https://www.graphpad.com/scientific-software/prism/</a>
MitoCarta 3.0	Broad Institute	<a href="https://www.broadinstitute.org/scientific-community/science/programs/metabolic-disease-program/publications/mitocarta/mitocarta-in-0">https://www.broadinstitute.org/scientific-community/science/programs/metabolic-disease-program/publications/mitocarta/mitocarta-in-0</a>
Panther	Geneontology	<a href="http://geneontology.org/">http://geneontology.org/</a>
Partek Genomics Suite V6.6	Partek	<a href="https://www.partek.com/partek-genomics-suite/">https://www.partek.com/partek-genomics-suite/</a>
Smart-seq2 workflow	Picelli et al., 2014	<a href="https://emea.illumina.com/science/sequencing-method-explorer/kits-and-arrays/smart-seq2.html">https://emea.illumina.com/science/sequencing-method-explorer/kits-and-arrays/smart-seq2.html</a>
TopHat2 version v2.0.11	Johns Hopkins University	<a href="https://ccb.jhu.edu/software/tophat/index.shtml">https://ccb.jhu.edu/software/tophat/index.shtml</a>

(Continued on next page)

**Continued**

REAGENT or RESOURCE	SOURCE	IDENTIFIER
Other		
Ketavet 100 mg/mL	Pfizer	6187926.00.00
Red Blood Cell Lysis Solution	Miltenyi Biotec	Cat# 130-094-183
Rompun 2%	Bayer	6293841.00.00
Tissue Tek O.C.T. Compound	Sakura Finetek	Cat# 4583

**RESOURCE AVAILABILITY**

**Lead contact**

Further information and requests for resources and reagents should be directed to and will be fulfilled by the lead contact, Sabine Eming ([sabine.eming@uni-koeln.de](mailto:sabine.eming@uni-koeln.de)).

**Materials availability**

*Dars2<sup>loxP/loxP</sup>* *Lyz2-cre* mice generated in this study are available from the lead contact upon request.

**Data and code availability**

- RNA-Seq and scRNA-Seq data have been deposited at GEO and are publicly available as of the date of publication. Accession numbers are: NCBI GEO: GSE157291; NCBI GEO: GSE183488, NCBI GEO: GSE183489. Original western blot images, flow cytometry data, and microscopy data reported in this paper will be shared by the lead contact upon request.
- This paper does not report original code.
- Any additional information required to reanalyze the data reported in this paper is available from the lead contact upon request.

**EXPERIMENTAL MODEL AND SUBJECT DETAILS**

**Mouse Models**

Animal housing and all the experimental procedures were authorized by the North Rhine–Westphalian State Agency for Nature, Environment, and Consumer Protection (LANUV, North Rhine–Westphalia, Germany) and the University of Cologne (84-02.04.2016.A030, 84-02.04.2017.A019, UniKöln\_Anzeige§4.16.018 to SAE). B6.RFP mice (ubiquitous RFP expression after germline excision of the *loxP*-flanked stop cassette; [Luche et al., 2007](#)) and C57BL/6JRj mice were housed in individually ventilated cages under SPF environment at the Experimental Center of the Medical Faculty, TU Dresden. For adoptive transfer experiments, wounding and cell transfer were conducted according to institutional guidelines and in accordance with the German Law for Protection of Animals approved by Landesdirektion Dresden (TVV 62/2015). All mouse lines used did not suffer from their gene modifications. Only mice which appeared healthy and were not involved in previous procedures were used for experiments. Mice were housed 2–5 per cage in a temperature (22–24°C) and humidity (relative humidity of 45–65 rH) controlled colony room, maintained on a 12 h light/dark cycle, with standard food (Altromin) and water provided *ad libitum*. The hygiene monitoring took place quarterly according to the recommendations of the FELASA (Federation of European Laboratory Animal Science Associations) for the health monitoring of laboratory animal facilities. The hygiene status of the animal husbandry was: SPF. *Dars2<sup>MKO</sup>* mice were generated by crossing *Dars2<sup>fl/fl</sup>* mice (C57BL/6N background, [Dogan et al., 2014](#)) with *Lyz2Cre* mice (C57BL/6N background, [Clausen et al., 1999](#)). *Il4ra<sup>MKO</sup>* mice (Balb/c background) were generated by crossing *Il4ra<sup>fl/fl</sup>* mice with *Lyz2Cre* mice as described previously ([Knipper et al., 2015](#); [Herbert et al., 2004](#)). All mice used in the experiments were generated by in-house mating except: C57BL/6J wild-type mice for wound healing experiments were purchased from Charles River and C57BL/6JRj wild-type mice for the adoptive cell transfer were purchased from Janvier. After importing the mice into the facility, they acclimatized for 1 week before starting the experiment. The sequences of the primers used to genotype the mice and to verify Cre-mediated recombination are provided in [Table S1](#). For wound healing studies, 8-to-12-week-old male or female mice were used for experiments. Animals were first allocated to different groups based on their genotype and then randomized for different time points of analysis. After wounding the animals were single-housed. For IL-4 complex-induced sterile peritonitis, 8-to-12-week-old male or female mice were used for experiments. Animals were first allocated to different groups based on their genotype and then randomized for injection with IL-4c or NaCl. Littermate controls were used by default in all experiments. The total number of mice analyzed for each experiment is detailed in the figure legends and in the respective methods section.

**Cell culture**

All cells were grown at 37°C in a 5% CO<sub>2</sub> humid atmosphere. Bone marrow cells were isolated from the femur and tibia of 8-to-20-week-old male or female mice. To generate BMDMs, bone marrow cells were seeded in non-coated 10 cm dishes in growth medium [DMEM cell culture medium supplemented with 10% fetal calf serum, 100 U/mL Penicillin, 0.1 mg/mL Streptomycin, 2 mM glutamine

(all Sigma-Aldrich), and M-CSF (20 ng/mL, Peprotech)]. Growth medium was exchanged every 3 days. After 12 days cells were harvested, counted, and seeded in 6-, 12- or 96-well plates (Sigma-Aldrich) for *in vitro* assays in a density of 250,000 cells/cm<sup>2</sup>. Specific treatment conditions for the different *in vitro* assays are specified in the [method details](#) section.

## METHOD DETAILS

### Excisional punch injury

Mice were anesthetized by intraperitoneal injection of 100 mg/kg body weight Ketavet (Pfizer) and 10 mg/kg bodyweight Rompun 2% (Bayer). The back skin was shaved using an electric shaver and disinfected with 70% ethanol. Full-thickness punch biopsies were created on the back using a standard biopsy puncher (Stiefel). For histological analysis, wounds were excised and processed following an established protocol ([Lucas et al., 2010](#); [Knipper et al., 2015](#); [Willenborg et al., 2012](#)). Thereby, wounds were excised at different times after injury and bisected in the caudocranial direction. The tissue was either fixed for 2 h in Roti®Histofix or embedded in O.C.T. compound (Fisher Scientific) and stored at -80°C. The manuscript shows data from a total of 15 independent wounding experiments.

### Adoptive transfer of RFP<sup>+</sup> monocytes

Whole bone marrow was isolated from female B6.RFP mice. Bone marrow cells were incubated with biotinylated antibodies against CD3 (diluted 1:200, eBioscience), CD4 (diluted 1:200, eBioscience), CD8 (diluted 1:400, eBioscience), CD45R (diluted 1:400, Biolegend), CD19 (diluted 1:200, eBioscience), NK1.1 (diluted 1:400, eBioscience), Ter119 (diluted 1:200, Biolegend), CD49b (diluted 1:200, Biolegend), Ly6G (diluted 1:200, Biolegend) and CD117 (diluted 1:200, Biolegend). Anti-Biotin microbeads (Miltenyi Biotec) were then used according to the manufacturer's protocol to isolate monocytes by immuno-magnetic depletion of biotin-labeled cells. Enrichment was validated by staining purified bone marrow monocytes with antibodies against CD115 (diluted 1:400, Biolegend) and Ly6C (diluted 1:200, BD Bioscience). For adoptive cell transfer, 3 x 10<sup>6</sup> monocytes were intravenously injected into each previously wounded C57/BL6JRj recipient, either 2 or 12 days after injury. Wounds were excised at 4 or 14 dpi.

### IL-4 complex-induced sterile peritonitis

Mice received i.p. injections (200 µL) of IL-4c containing 5 µg of IL-4 (Peprotech) and 25 µg of anti-IL-4 (BioXcell) or NaCl vehicle control on days 0 and 2 ([Jenkins et al., 2011](#)). Peritoneal cells were harvested at day 4 by flushing the peritoneal cavity with 8 mL PBS (peritoneal lavage). 1 x 10<sup>6</sup> or 2 x 10<sup>6</sup> CD45<sup>+</sup>CD11b<sup>+</sup>F4/80<sup>+</sup> peritoneal cells were sorted by flow cytometry and subjected to Western blot analysis and qRT-PCR analysis, respectively. In total 4 independent experiments were performed.

### Morphometric analysis

Morphometric analysis was performed on H&E-stained paraffin tissue sections using light microscopy equipped with a KY-F75U digital camera (JVC) at various magnifications (Leica DM4000B, Leica Microsystems; Diskus 4.50 software) as described previously ([Lucas et al., 2010](#); [Knipper et al., 2015](#); [Willenborg et al., 2012](#)). The extent of granulation tissue formation and the amount of fibrin-rich granulation tissue were assessed. The gap between the epithelial tips was determined as a measure of wound closure. Analysis was performed in a blinded manner. Two independent wounding experiments were performed.

### Immunostaining

For CD31 immunofluorescence staining, cryostat sections (10 µm thick) from OCT embedded tissues were fixed in acetone (stored at -20°C) for 5 min, washed in PBS 3 times, and blocked in 10% normal goat serum in PBS for 1 h at RT. Slides were incubated with anti-CD31 (BD Biosciences), diluted 1:50 in blocking buffer, overnight at 4°C. After 3 washes bound primary antibodies were detected by Alexa Fluor 488-conjugated secondary antibody (Thermo Fisher Scientific), followed by counterstaining with DAPI (Invitrogen). After three washes, slides were covered with coverslips in mounting medium (glycerol gelatine). Stained sections were analyzed using the Keyence BZ-9000 fluorescence microscope and the BZ-II viewer software. Photographs were further processed with Adobe Photoshop 7.0 (Adobe Systems) and the relative proportion of the CD31<sup>+</sup> area per hpf was analyzed with ImageJ. Analysis was performed in a blinded manner. Two independent wounding experiments were performed.

### Flow cytometry

Single-cell suspensions of wound tissue were prepared by a combination of enzymatic digestion (Liberase Blendzyme, Roche Applied Science) and mechanical disruption (Medimachine System, BD Biosciences). Excised wound tissue was sectioned with a scalpel, placed in DMEM medium supplemented with 30 µg/mL Liberase TM Research Grade (Roche), and incubated at 37°C for 90 min (shaking). Digested wound tissue was mechanically disrupted for 5 min using the Medimachine System (BD Biosciences). Cells were passed through 70 µm and 40 µm cell strainer, and washed with ice-cold PBS/1% BSA/2 mM EDTA. Leukocytes were isolated from whole blood by hypotonic lysis of erythrocytes using Red Blood Cell Lysis Solution (Miltenyi Biotec) followed by ice-cold PBS/1% BSA/2 mM EDTA washes. Fc receptors were blocked with anti-CD16/CD32 (diluted 1:50, Thermo Fisher Scientific) and cells were stained with fluorescein isothiocyanate (FITC)-conjugated anti-CD45 (diluted 1:200, Thermo Fisher Scientific), allophycocyanin (APC)-conjugated or APC-Cy7-conjugated anti-CD11b (diluted 1:300, Thermo Fisher Scientific), phycoerythrin (PE)-conjugated anti-F4/80 (diluted 1:50, Bio-Rad Laboratories), and APC-conjugated anti-CD115 (diluted 1:300, Thermo Fisher Scientific) in

PBS/1% BSA/2 mM EDTA. Dead cells were excluded using 7-AAD or DAPI (Thermo Fisher Scientific). Cells were analyzed using a FACSCanto II flow cytometer (BD) and sorted using a FACSARIA III cell sorting system (BD Biosciences) equipped with FACSDiva Version 6.1.1 software (BD Biosciences). FACS data were further analyzed by FlowJo Version 10.7.1 (FlowJo).

### Western blot analysis

For analysis of HIF-1 $\alpha$ , BMDMs were pretreated with 5 mM Diethylsuccinate (Sigma-Aldrich) in growth medium for 3 h, followed by stimulation with 100 ng/mL LPS (Sigma-Aldrich) for 48 h. After 3 washes with PBS (4°C) cells were lysed in 50 mM Tris/HCl pH 7.5, 150 mM NaCl, 1% Triton-X-100, and 0.1% SDS buffer containing protease inhibitor (Sigma-Aldrich) and phosphatase inhibitor (Roche). For flow cytometry-sorted wound cells, at 4 dpi, 8 wounds from 2 mouse were pooled. At 14 dpi, 20–24 wounds from 5–6 mice were pooled. Sorted cells were lysed in the same buffer as for BMDMs. Samples were passed ten times through a syringe needle to obtain whole cell lysates. Protein concentration was determined by the Micro BCA Protein Assay Kit (Thermo Fisher Scientific). 10  $\mu$ g protein per sample were subjected to SDS-PAGE. Subsequently, protein was blotted onto PVDF membranes. After blocking in 5% non-fat milk in TBST buffer or for HIF-1 $\alpha$  in ROTI®Block for (Roth), membranes were incubated over night at 4°C with primary antibodies: total OXPHOS Rodent WB Antibody Cocktail (diluted 1:2,000, Abcam), anti-OxPhos Complex IV subunit IV (diluted 1:2,000, ThermoFisher Scientific), anti- $\beta$ -actin (diluted 1:1,000, Sigma-Aldrich), anti-HIF-1  $\alpha$  (diluted 1:2,000, Novus Biologicals), and anti-DARS2 (diluted 1:1,000, Proteintech). After 3 washes membranes were incubated with the appropriate HRP-conjugated secondary antibody (diluted 1:1,000) for 1 h at RT. Membranes were developed using ECL substrate (PerkinElmer). Bands were visualized using the AGFA Curix 60 developing machine. Three independent experiments were performed.

### Analysis of mitochondrial mass

BMDMs were seeded in 6-well plates (Sigma-Aldrich) in a density of 250,000 cells/cm<sup>2</sup> in growth medium. Cells were stimulated with IL-4 + IL-13 (200 ng/mL each) or vehicle for 48 h. Medium was exchanged with DMEM containing MitoTracker™ Green (1:7,500; Thermo Fisher Scientific) and cells were incubated for 15 min at 37°C. Cells were centrifuged and the pellet was resuspended in DMEM and incubated for 15 min at 37°C. Cells were centrifuged, resuspended in PBS/1% BSA/2 mM EDTA, and stained with eFluor450-conjugated anti-CD45 (diluted 1:200, Thermo Fisher Scientific), APC-conjugated anti-CD11b (diluted 1:300, Thermo Fisher Scientific) and PE-conjugated anti-F4/80 (diluted 1:50, Bio-Rad Laboratories). CD11b<sup>+</sup>F4/80<sup>+</sup> wound macrophages were flow cytometry-sorted (200,000 cells/sample; 4 dpi: 4 wounds from 1 one mouse were pooled; 14 dpi: 8 wounds from 2 mice were pooled) and cells were incubated with MitoTracker™ Green as described above. Dead cells were excluded using 7-AAD. Mean fluorescence intensity in the FITC channel in the gate of CD45<sup>+</sup>CD11b<sup>+</sup>F4/80<sup>+</sup> BMDMs or CD11b<sup>+</sup>F4/80<sup>+</sup> wound cells was used as a measure of mitochondrial mass. At least two independent experiments were performed.

### Analysis of mitochondrial reactive oxygen species

BMDMs were harvested and resuspended in Hank's balanced salt solution with calcium and magnesium (HBSS/Ca/Mg, Gibco). From this, 1 million cells were incubated with 1 mL of 2.5  $\mu$ M MitoSOX™ Red mitochondrial superoxide indicator (Thermo Fisher Scientific) in HBSS for 10 min at 37°C. Cells were washed in HBSS twice and resuspended in HBSS containing 200 ng/mL LPS or vehicle for 2 h. The proportion of MitoSOX<sup>+</sup> cells was determined in the PE-channel using a FACSCanto II (BD Biosciences). The ratio of MitoSOX<sup>+</sup> LPS-treated cells over vehicle-treated cells was determined. Two independent experiments were performed.

### Analysis of mitochondrial membrane potential by TMRM

BMDMs were seeded in 12-well plates in a density of 250,000 cells/cm<sup>2</sup> in growth medium and stimulated with LPS (100 ng/mL) or vehicle for 48 h. After 48 h medium was exchanged with growth medium supplemented with 100 nM TMRM followed by incubation for 30 min at 37°C and 5% CO<sub>2</sub>. Cells were washed twice with PBS (37°C) followed by adding PBS/0.02% EDTA (37°C). Cells were scraped off and stained in PBS/2%FCS/2 mM EDTA with anti-CD45-FITC (diluted 1:200) and anti-CD11b-APC (diluted 1:300, Thermo Fisher Scientific). DAPI (50 ng/mL) was used for live/dead discrimination. DAPI<sup>+</sup>CD45<sup>+</sup>CD11b<sup>+</sup> single cells were gated and the mean fluorescence intensity in the PE channel was determined as a measure of the mitochondrial membrane potential. Oligomycin (1  $\mu$ M) and FCCP (15  $\mu$ M) were used as positive and negative control, respectively. A FACSCanto II cytometer (BD) was used for the analysis. Three independent experiments were performed.

### Enzyme histochemistry to follow COX and SDH activities

BMDMs were seeded in chamber slides (Thermo Fisher Scientific) in growth medium overnight. Medium was discarded, cells put on ice, and washed 3 times with PBS (4°C) and once with H<sub>2</sub>O. Cells were air-dried for 25 min at RT and then incubated with 5 mM diaminobenzidine tetrahydrochloride, 500  $\mu$ M cytochrome c, and catalase (Sigma-Aldrich) at 37°C for 1 h min to follow COX activity. Cells were washed with PBS and incubated at 37°C for 2.5 h with 1.875 mM nitroblue tetrazolium, 1.30 M sodium succinate, 2.0 mM phenazine methosulfate, and 100 mM sodium azide (Sigma-Aldrich) to follow SDH activity. Slides were dehydrated with graded alcohols, air-dried, and mounted with Pertex. Two independent experiments were performed.

### Analysis of extracellular flux

Analyses of OCR and ECAR were performed using the Seahorse extracellular flux analyzer Xfe 96 (Agilent). BMDMs were seeded in growth medium into XF 96-well cell culture microplates (80,000 cells per well) and allowed to recover for 16 h. Medium was



exchanged with buffer-free Assay Medium (Seahorse Bioscience) and cells were then transferred to a CO<sub>2</sub>-free incubator and maintained at 37°C for 1 h before starting the assay. CD45<sup>+</sup>CD11b<sup>+</sup>F4/80<sup>+</sup> wound macrophages were flow cytometry-sorted, collected in buffer-free Assay Medium (Seahorse Bioscience), and seeded into XF 96-well cell culture microplates (80,000 cells per well). At 4 dpi cells from 24 wounds and 6 mice per genotype were pooled; at 14 dpi cells from 48 wounds and 12 mice per genotype were pooled. Cells were transferred to a CO<sub>2</sub>-free incubator and maintained at 37°C for 1 h before starting the assay. Following instrument calibration, cells were transferred to the XF24 Flux Analyzer to record cellular OCRs and ECARs. The measurement protocol consisted of 2 min mixture, 2 min wait, and 4 min OCR measurement times. For the mitochondrial stress test, ATP synthase was inhibited by injection of 1 mM oligomycin, followed by 3 mM FCCP to induce mitochondrial uncoupling to determine the spare/maximal respiratory capacity. Non-mitochondrial respiration was determined after rotenone/antimycin A injection (1 mM each). At the end of the assay, the medium was carefully aspirated and cellular DNA measured using CyQuant (Thermo Fisher Scientific) to adjust for potential differences in cell densities. Three independent experiments were performed.

### Isolation of mitochondria

12 × 10<sup>6</sup> cultured BMDMs were used for isolation of mitochondria. Cells were resuspended in 20 mM HEPES pH 7.6, 220 mM mannitol, 70 mM sucrose, 1 mM EDTA, 0.2% fatty acid-free BSA, and homogenized with a glass-glass hand homogeniser (Kontes Tissue Grinder, Thomas Scientific) for 25 strokes, followed by differential centrifugation at 850 × g, and 8500 × g, 5 min, 4 °C. Isolated mitochondria were resuspended in 20 mM HEPES pH 7.6, 220 mM mannitol, 70 mM sucrose, 1 mM EDTA.

### Blue native polyacrylamide gel electrophoresis (BN-PAGE) and in-gel activity

Mitochondrial protein concentrations were determined with Bradford reagent (Sigma). 20 µg of mitochondrial proteins were lysed for 15 min on ice in dodecylmaltoside (5 g/g of protein) and cleared from insoluble material for 30 min at 20,000 × g, 4 °C. BN-PAGE was carried out using the NativePAGE Novex Bis-Tris Mini Gel system (Thermo Fisher Scientific) according to the manufacturer's specifications. Separated mitochondrial complexes were transferred onto a polyvinylidene fluoride membrane using the wet transfer methanol-free system. Membranes were incubated with the following antibodies: Mouse monoclonal anti-ATP5A 1:1000, anti-UQCRC1 1:1000, anti-MT-CO1 1:1000, anti-SDHA 1:5000, anti-NDUFA9 1:1000. Signal was developed with ECL-based signal detection. Complex I in-gel activity was measured by incubating BN-PAGE gel in NADH 0.1 mg/mL and nitroretazolium blue 2.5 mg/mL in 5 mM Tris (pH 7.4) for 1 h, as described previously (Dogan et al, 2014). At least two independent experiments were performed.

### Quantitative Real-time PCR analysis

For *in vitro* gene expression analysis, cells were seeded in 96-well plates. Growth medium was exchanged with growth medium supplemented with either LPS + IFN $\gamma$  (each 50 ng/mL, Sigma-Aldrich, Peprotech) or IL 4 + IL 13 (each 50 ng/mL, Peprotech), or vehicle (growth medium) for 5 h or 24 h. After stimulation cells were washed 3 times with PBS (4 °C) and lysed in 350 µL RLT lysis buffer (Qiagen). For wound macrophages and blood monocytes, 2 × 10<sup>5</sup> flow cytometry-sorted CD45<sup>+</sup>CD11b<sup>+</sup>F4/80<sup>+</sup> cells were lysed in 350 µL RLT lysis buffer (Qiagen). Total RNA was isolated using the RNeasy Plus Micro or Mini Kit (Qiagen) according to the manufacturer's instructions. At 4 dpi 4 wounds from 1 mouse were pooled; at 14 dpi 8 wounds from 2 mice were pooled. Reverse transcription of isolated RNA was performed using the High Capacity cDNA RT Kit (Thermo Fisher Scientific). Amplification reactions (triplicates) were set up using the PowerSYBR Green PCR Master Mix (Thermo Fisher Scientific) and qRT-PCR was performed using the QuantStudio™ 5 Real-time PCR system (Thermo Fisher Scientific). The comparative method of relative quantification (2<sup>- $\Delta\Delta C_t$</sup> ) was used to calculate the expression level of the target gene normalized to a housekeeping gene (*Rps29* or *Rps18*). All primer sequences are listed in Table S1. Three independent wounding experiments were performed.

### Bulk RNA sequencing of wound macrophages

#### Wounding and preparation of wound tissue

Full thickness punch biopsies were inflicted in the back skin of C57BL/6J wild-type mice. CD45<sup>+</sup>CD11b<sup>+</sup>F4/80<sup>+</sup> wound cells at 4 and 14 dpi were sorted by flow cytometry and subjected to quantitative RNA sequencing. At 4 dpi, 4 independent samples were analyzed with each sample representing 6 × 10<sup>5</sup> CD45<sup>+</sup>CD11b<sup>+</sup>F4/80<sup>+</sup> cells pooled from 8 wounds of 2 mice, whereas at 14 dpi, 5 independent samples were analyzed with each sample representing 3 × 10<sup>5</sup> CD45<sup>+</sup>CD11b<sup>+</sup>F4/80<sup>+</sup> cells pooled from 12 wounds of 3 mice. After sorting, cells were lysed in TRIzol (Thermo Fisher Scientific). Total RNA was extracted according to the manufacturer's protocol and the precipitated RNA was dissolved in RNase-free water. The quality of the RNA was assessed by measuring the ratio of absorbance at 260 nm and 280 nm using a Nanodrop 2000 Spectrometer (Thermo Fisher Scientific) as well as by visualizing the integrity of the 28S and 18S bands on an agarose gel.

#### Generation of cDNA libraries

Total RNA was converted into libraries of double-stranded cDNA molecules as a template for high throughput sequencing following the manufacturer's recommendations using the Illumina TruSeq RNA Sample Preparation Kit v2. In brief, mRNA was purified from 100 ng of total RNA using poly-T oligo-attached magnetic beads. Fragmentation was carried out using divalent cations under elevated temperatures in Illumina proprietary fragmentation buffer. First strand cDNA was synthesized using random oligonucleotides and SuperScript II. Second strand cDNA synthesis was subsequently performed using DNA Polymerase I and RNase H. Remaining overhangs were converted into blunt ends via exonuclease/polymerase activities and enzymes were removed. After

adenylation of 3' ends of DNA fragments, Illumina PE adapter oligonucleotides were ligated to prepare for hybridization. DNA fragments with ligated adapter molecules were selectively enriched using Illumina PCR primer PE1.0 and PE2.0 in a 15 cycle PCR reaction. Size-selection and purification of cDNA fragments with preferentially 200 bp in length was performed using SPRIbeads (Beckman-Coulter). The size-distribution of cDNA libraries was measured using the Agilent high sensitivity DNA assay on a Bioanalyzer 2100 system (Agilent). cDNA libraries were quantified using KAPA Library Quantification Kits (Kapa Biosystems). After cluster generation on a cBot, a 2 × 100 bp paired-end run was performed on a HiSeq1500.

### **RNA-seq preprocessing**

After base calling and de-multiplexing using CASAVA version 1.8, the 100 bp paired-end reads were aligned to the murine reference genome mm10 from UCSC by TopHat2 version v2.0.11 and Bowtie2 version 2.2.1 using the default parameters. This annotation included 32,600 unique transcript entries with genomic coordinates. After mapping of the reads to the genome, we imported the data into the Partek Genomics Suite V6.6 (PGS) to calculate the number of reads mapped to each transcript against the RefSeq mm10 annotation download in April 2014. These raw read counts were used as input to DESeq2 for calculation of normalized signal for each transcript using the default parameters. After DESeq2 normalization, the normalized read counts were imported back into PGS and floored by setting all read counts to at least a read count of 1 after the batch correction. Subsequent to flooring, all transcripts having a maximum over all group mean lower than 10 were removed. After dismissing the low expressed transcripts, the data comprised 13,674 transcripts. RNA-seq data can be accessed under NCBI GEO: GSE157291.

### **Statistical and descriptive bioinformatics of transcriptome data**

A one-way Analysis Of VAriance (ANOVA) model was performed to calculate the 1,000 genes having the highest variance and the differentially expressed genes between early and late phase wound macrophages using PGS. Differentially expressed genes were defined by a fold change (FC) > 2.0 or < - 2.0 and a false discovery rate (FDR) corrected p-value < 0.05. To visualize the structure within the data, we performed PCA on all genes and HC on the 1,000 genes having the highest variance, with default settings in PGS, based on p-values according to the expression values of the samples across the conditions. To identify the differences and similarities between early- and late-phase wound macrophages, the differentially expressed genes were visualized with R as a ratio-ranked (log<sub>2</sub>) plot. To link differentially expressed genes to mitochondrial functions, we compared the differentially expressed genes with MitoCarta 3.0 data sets and gene ontology enrichment analysis was performed using PANTHER.

### **Single-cell RNA sequencing of wound macrophages**

Wound cells were isolated from C57BL/6J wild-type mice and stained for flow cytometry as described above. Dead cells were excluded by labelling them with 50 ng/mL DAPI (Thermo Fisher Scientific). Single CD45<sup>+</sup>CD11b<sup>+</sup>F4/80<sup>+</sup> cells from wounded skin were index-sorted (BD FACS Aria II SORP) into 384 well plates containing 0.5 µL of nuclease free water with 0.2% Triton-X 100 and 4 U murine RNase Inhibitor (NEB), spun down and frozen at -80°C. Libraries were prepared following the Smart-seq2 workflow (Picelli et al., 2014). Briefly, after thawing, 0.5 µL of a primer mix were added (5 mM dNTP (Invitrogen), 0.5 µM dT-primer (C6-amino-linker-AAGCAGTGGTATCAACGCAGAGTCGACTTTTTTTTTTTTTTTTTTTTTTTTTTTT), 1 U RNase Inhibitor (NEB)). RNA was denatured for 3 minutes at 72°C and the reverse transcription (RT) was performed at 42°C for 90 min after filling up to 10 µL with RT buffer mix for a final concentration of 1x superscript II buffer (Invitrogen), 1 M betaine, 5 mM DTT, 6 mM MgCl<sub>2</sub>, 1 µM TSO-primer (AAGCAGTGGTATCAACGCAGAGTACATrGrGrG), 9 U RNase Inhibitor and 90 U Superscript II. After synthesis, the reverse transcriptase was inactivated at 70°C for 15 min. The cDNA was amplified using Kapa HiFi HotStart Readymix (Peqlab) at a final 1x concentration and 0.1 µM UP-primer (AAGCAGTGGTATCAACGCAGAGT) under following cycling conditions: initial denaturation at 98°C for 3 min, 23 cycles [98°C 20 sec, 67°C 15 sec, 72°C 6 min] and final elongation at 72°C for 5 min. The amplified cDNA was purified using 1x volume of hydrophobic Sera-Mag SpeedBeads (GE Healthcare) resuspended in a buffer consisting of 10 mM Tris, 20 mM EDTA, 18.5 % (w/v) PEG 8000 and 2 M sodium chloride solution. The cDNA was eluted in 12 µL nuclease free water and the concentration of the samples was measured with a Tecan plate reader Infinite 200 pro in 384 well black flat bottom low volume plates (Corning) using AccuBlue Broad range chemistry (Biotium).

For library preparation up to 700 pg cDNA was desiccated and rehydrated in 1 µL Tagmentation mix (1x TruePrep Tagment Buffer L, 0.1 µL TruePrep Tagment Enzyme V50; from TruePrep DNA Library Prep Kit V2 for Illumina; Vazyme) and tagmented at 55°C for 5 min. Subsequently, Illumina indices were added during PCR (72°C 3 min, 98°C 30 sec, 13 cycles [98°C 10 sec, 63°C 20 sec, 72°C 1 min], 72°C 5 min) with 1x concentrated KAPA HiFi HotStart Ready Mix and 300 nM dual indexing primers. After PCR, libraries were quantified with AccuBlue Broad range chemistry, equimolarly pooled and purified twice with 1x volume Sera-Mag SpeedBeads. This was followed by Illumina 50 bp paired-end sequencing on a Novaseq6000 aiming at an average sequencing depth of 0.5 mio reads per cell.

Raw reads were mapped to the mouse genome (GRCm38) and splice-site information from Ensembl release 87 with gsnap v.2018-07-04 (Wu and Nacu, 2010). Uniquely mapped reads and gene annotations from Ensembl release 87 were used as input for featureCounts v. 1.6.2 (Liao et al., 2014) to create counts per gene and cell. Read count matrices were processed, analyzed and visualized in R v. 4.0.0 (R Core Team, 2013) using Seurat v. 3 (Stuart et al., 2019) with default parameters in all functions, unless specified. Poor quality cells, with low total unique molecular identifier (UMI) counts and high percent mitochondrial gene expression or reads mapping to ERCC spike-in controls, were excluded. Filtered samples were normalized using a regularized negative binomial regression (SCTransform) (Hafemeister and Satija, 2019) and integrated with the reciprocal PCA (rpca) approach followed by mutual nearest neighbors, using 50 principal components. Integrated gene expression matrices were visualized with a Uniform Manifold Approximation and Projection (UMAP) (McInnes et al., 2018) as a dimensionality reduction approach. Resolution for cell clustering

was determined by evaluating hierarchical clustering trees at a range of resolutions (0 - 1.2) with Clustree (Zappia and Oshlack, 2018), selecting a value inducing minimal cluster instability. Differentially expressed genes between clusters were identified as those expressed in at least 25% of cells with a greater than +0.25 log fold change and an adjusted p value of less than 0.01, using the FindMarkers function in Seurat v.3 with all other parameters set to default. Ribosomal protein genes were excluded from results. Gene set scores were calculated using the AddModuleScore function in Seurat v.3 with default parameters. Briefly, the average expression levels of each identified gene set was calculated on a single cell level and subtracted by the aggregated expression of randomly selected control gene sets. For this purpose, target genes are binned based on averaged expression, and corresponding control genes are randomly selected from each bin. 381 cells at 4 dpi and 680 cells at 14 dpi were analyzed. Two independent experiments were performed. scRNA-Seq data can be accessed under NCBI GEO: GSE183489.

### RNA sequencing in BMDMs

BMDMs were seeded in 12-well plates (Sigma-Aldrich) in a density of 250,000 cells/cm<sup>2</sup> in growth medium. Cells were stimulated with IL-4+IL-13 (50 ng/mL each) or vehicle for 48 h. Cells were washed twice in PBS (4°C) and lysed in RLT lysis buffer (Qiagen). Total RNA was isolated using the RNeasy Plus Mini Kit (Qiagen) according to the manufacturer's instructions. Libraries were prepared using the Illumina® Stranded TruSeq® RNA sample preparation Kit. Library preparation started with 2 µg total RNA. After poly-A selection (using poly-T oligo-attached magnetic beads), mRNA was purified and fragmented using divalent cations under elevated temperature. The RNA fragments underwent reverse transcription using random primers. This was followed by second strand cDNA synthesis with DNA Polymerase I and RNase H. After end repair and A-tailing, indexing adapters were ligated. The products were then purified and amplified (14 PCR cycles) to create the final cDNA libraries. After library validation and quantification (Agilent 2100 Bioanalyzer), equimolar amounts of library were pooled. The pool was quantified by using the Peqlab KAPA Library Quantification Kit and the Applied Biosystems 7900HT Sequence Detection System. The pool was sequenced on an Illumina NovaSeq6000 sequencing instrument with PE100 protocol.

Sequenced libraries were processed in an in-house developed RNA sequencing pipeline (Bhardwaj et al., 2019) that employs deepTools for quality control (Ramirez et al., 2016), cutadapt for trimming (Martin, 2011), STAR (Dobin et al., 2013) for mapping, and featureCounts (Liao et al., 2014) to quantify mapped reads. Raw counts of mapped reads were processed in R v. 3.6.3 (Lucent Technologies) with DESeq2 v.1.28.1 to determine differentially expressed genes. RNA-Seq data can be accessed under NCBI GEO: GSE183488.

## QUANTIFICATION AND STATISTICAL ANALYSIS

### Data representation and statistical analysis

In the wound healing model and the IL-4c-induced peritonitis model the required sample size was computed *a priori* using G\*Power 3.1.9.2. The analysis of wound sections (assessment of gt, fibrin-rich area, CD31<sup>+</sup> area) was performed in a blinded fashion. Mice shall be excluded from wound healing experiments or from IL-4c-induced peritonitis experiments when the burden after the treatment exceeds a defined level (based on LANUV guidelines). In this study no mouse had to be excluded.

Specific information about how many wounds were pooled for the cell sorting of wound macrophages is provided in the respective [method details](#) sections. Data are displayed as dot plots, which include each datapoint and the mean value displayed as a bar. In case of extracellular flux experiments, the mean value ± SEM is represented. Results of visual inspection of continuous data distributions and formally testing using the Kolmogorov Smirnov test were consistent with "normality" (i.e.  $P > 0.1$ ). Thus, parametric methods, i.e. Student's unpaired two-tailed t- test (when 2 groups were compared) or one-way ANOVA with Tukey's post-test (when more than 2 groups were compared) were used (GraphPad Prism 8 software). In case of not assumed equal variances, a Welch correction was performed. scRNA-seq data were analyzed using a 2 factor ANOVA first, with both the clusters and conditions (4 dpi and 14 dpi) as factors, followed by Tukey's 'Honest Significant Difference' method to determine the significance of the condition effect. All  $P$  values and  $n$  are reported in the figure legends. Results are considered significant when  $P < 0.05$ .